Low-to-moderate Reynolds number swirling flow in an annular channel with a rotating end wall

Laurent Davoust, Jean-Luc Achard, and Laurent Drazek

Phys. Rev. E **91**, 023019 — Published 27 February 2015

DOI: 10.1103/PhysRevE.91.023019

Low-to-moderate Reynolds number swirling flow in an annular channel with a rotating end wall.

Laurent Davoust*
Grenoble-INP, SIMaP, Electromagnetic Processing of Materials (EPM) Laboratory, F-38000 Grenoble, France

Jean-Luc Achard
CNRS, LEGI, Microfluidics, Particles and Interfaces (MIP) Laboratory, F-38000 Grenoble, France

Laurent Drazek
Univ. Grenoble Alpes, LEGI, Microfluidics, Particles and Interfaces (MIP) Laboratory, F-38000 Grenoble, France†

This paper presents a new method for solving analytically the axisymmetric swirling flow generated in a finite annular channel from a rotating end wall, with no-slip boundary conditions along stationary side walls and a slip condition along the free surface opposite the rotating floor. In this case, the end-driven swirling flow can be described from the coupling between an azimuthal shear flow and a two-dimensional meridian flow driven by the centrifugal force along the rotating floor. A regular asymptotic expansion based on a small but finite Reynolds number is used to calculate centrifugation-induced first-order correction to the azimuthal Stokes flow obtained as the solution at leading order. For solving first-order problem, the use of an integral boundary condition for the vorticity is found to be a convenient way to attribute boundary conditions in-excess for the stream function to the vorticity. The annular geometry is characterized by both vertical and horizontal aspect ratios, whose respective influences on flow patterns are investigated. The vertical aspect ratio is found to involve non-trivial changes in flow patterns essentially due to the role of corner eddies located on the left and right sides of the rotating floor. The present analytical method can be ultimately extended to cylindrical geometries, irrespective of the surface opposite the rotating floor: a wall or a free surface. It can also serve as an analytical tool for monitoring confined rotating flows in applications related to surface viscosimetry or crystal growth from the melt.

PACS numbers: 47.10.-g; 47.15.-x; 47.32.-y; 68.03.-g
Keywords: Rotating flow; end-driven flow; swirl; regular perturbation; integral vorticity condition; stream function

---

* laurent.davoust@simap.grenoble-inp.fr
† bioMérieux, Technology Research Dpt., Centre Christophe Mérieux, 38024 Grenoble, France

I. INTRODUCTION

Viscous incompressible flows inside cylindrical containers with a rotating end wall and a free surface above have received sustained attention (see e.g. [1–8] as a non-exhaustive shortlist of references), motivated by both their fundamental and engineering relevance. Taking advantage of the simplicity of the cylindrical geometry, several analytical models based on a low Reynolds number limit [9–11] have been developed. Moreover, different boundary conditions applied to the liquid surface opposite the rotating end wall (free surface, contaminated surface, solid wall, rotating cover) have been considered, allowing for meaningful comparisons between analytical approaches, experimental data and numerical calculations. Fundamental interest essentially focuses on the Ekman pumping which, given a high enough Reynolds number and a particular range of the only available length-to-radius aspect ratio, leads to the formation or breakdown of a concentrated vortex bubble along the axis.

In a similar way, the flow in a cylindrical annular channel (Fig. 1) should also be investigated. The main reason for this is that its geometry is generic in the sense that, depending on the limiting value of the ratio of the inner radius over the outer radius, r_i/r_o, the geometry of a straight channel can be approached. Despite both its fundamental interest and its relevance in applications related to crystal growth[12] or surface viscosimetry [13–15], it is surprising to see how end-driven annular flows have not attracted as much attention as full cylinders. Most existing studies on annular channel flows have been performed numerically or experimentally [13, 15–17], quite often with the aim of investigating the impact of physicochemical contamination along the upper liquid surface. To our knowledge, except for the recent analytical modeling performed by Shtern [18, 19] for an annular cavity considered as semi-infinite along the vertical direction, all existing analytical studies devoted to this configuration only focus on the azimuthal flow either when the liquid surface is free of contamination [20] or when it is contaminated [21, 22].

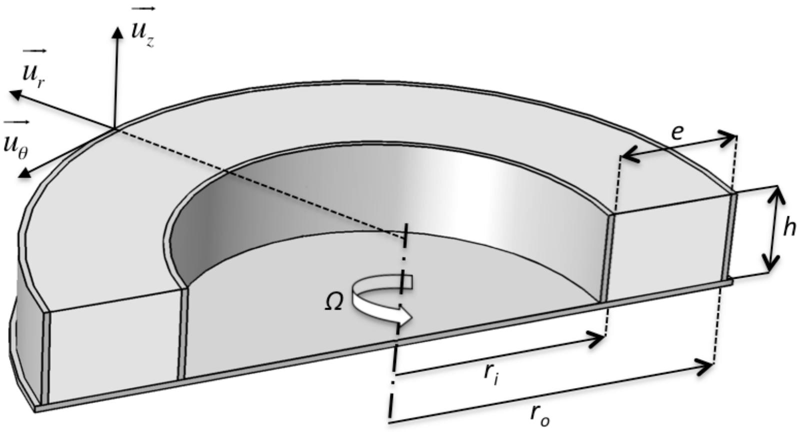

Figure 1. Partial view of the channel geometry under consideration. The floor is rotating slowly while the inner and outer side walls (at r_i and r_o respectively) are maintained stationary.

The primary purpose of the present study is therefore to remedy this gap, i.e. to understand the role of inertial correction to the azimuthal Stokes flow in a finite annular cavity with a rotating end wall and a free surface above. To this end, a new analytical method is proposed, which can address a diversity of boundary conditions around the fluid domain (stationary side walls, moving wall, free surface). The Reynolds number considered here is small but finite, which means that it ranges between the Stokes limit (Re = 0) and the weakly inertial flow (Re $\sim$ 100 typically). Beyond this limit, as already mentioned, flow topology is well documented by direct numerical studies carried out by Lopez and co-workers ([16, 17]).

Furthermore, our approach will show how flow patterns evolve according to the vertical and horizontal aspect ratios, especially when the vertical aspect ratio is small (radially-extended cavity).

As a typical property of end-driven flows, discontinuities are found at the left and right corners, between the rotating floor and the inner side wall, maintained stationary, or between the rotating floor and the outer side wall, also maintained stationary. It is therefore difficult to use Stokes solutions to tackle these boundary discontinuities, as the associated Stokes series for the stream function diverge when differentiated. This problem cannot be circumvented since our aim is precisely to calculate the recirculating flow induced by centrifugation within a meridian cross-section of the annular channel. In the present paper, we propose an analytical method based on the systematic use of dot products so that involved analytical series can always be integrated. In this way, the viscous impact of boundary discontinuities upon the flow can be described.

The outline of the paper is as follows. In section II.A, the entire flow is split between the azimuthal flow and the recirculating flow in the meridian plane, where the latter is described from non-primitive variables: the stream function and the vorticity. The three governing equations for the entire flow are obtained, all based on the same single differential operator. In section II.C, to demonstrate how the azimuthal flow and the meridian flow are weakly coupled, use is made of a regular perturbation series based on a low Reynolds number. Three eigenvalue problems are derived, associated with governing equations. In section II.D, an integral boundary condition is introduced to deal with in-excess boundary conditions for the stream function. Then, in section II.E, the solutions at successive orders are derived. Special attention is given to the method for solving the inertial correction at first-order to the azimuthal Stokes flow. In section III.A, the accuracy of the analytical method is discussed, focusing particularly on the azimuthal flow calculated up to second-order. The influence of corner discontinuities is also discussed. Finally, in the section III.B, special attention is dedicated to analyzing the 2-D cellular flow induced by centrifugation and perturbed by corner singularities.

II. MATHEMATICAL FORMULATION

A. Governing equations

This paper addresses the permanent flow of an incompressible fluid with a free surface in a cylindrical lid driven annulus between a couple of vertical cylindrical and stationary side walls with inner and outer diameters, r_i and r_o, respectively. The floor at the bottom of the cavity is made to rotate slowly. Figure 1 shows the geometry of the annulus and the coordinate system, where r is taken along the radial direction and z along the vertical direction. All physical quantities are normalized by taking outer radius r_o as the representative length scale and $1/\Omega$ as the time-scale, where Ω is the rotation speed rate of the floor. The non-dimensional Reynolds number is consistently defined by $Re = \frac{\rho r_o^2 \Omega}{\mu}$ with ρ and μ, the density and the newtonian viscosity of the liquid.

In this paper, the swirling flow under consideration is characterized by a cylindrical symmetry. A distinction is made between a main azimuthal flow, described by the primitive variable, $\overrightarrow{v_\theta} = v_\theta\left(r,z\right)\overrightarrow{u_\theta}$, and a two-dimensional recirculating flow within a meridian cross-section, $\overrightarrow{v_\perp} = v_r\left(r,z\right)\overrightarrow{u_r} + v_z\left(r,z\right)\overrightarrow{u_z}$, the components (v_r, v_z) of which are derived from the following non-primitive variables: the vorticity function ω and the stream function ψ which differs from the well-known Stokes function[1]: here, the 2-D meridian velocity writes, $\overrightarrow{v_\perp} = \nabla\times(\psi\overrightarrow{u_\theta})$, or explicitly:

$$v_r = -\frac{\partial\psi}{\partial z}, \tag{1}$$

$$v_z = \frac{1}{r}\frac{\partial\left(r\psi\right)}{\partial r}. \tag{2}$$

Hence, the continuity equation is satisfied and, anticipating on the following, the latter non primitive formulation permits the use of only one single generic differential operator, E^2, in the writing of the following mathematical modeling (4)-(6) with inertia appearing in the form of source terms.

Dependence of the vorticity ω on $\overrightarrow{v_\perp}$ is written as:

$$\omega = \overrightarrow{u_\theta}.\left(\overrightarrow{\nabla}\times\overrightarrow{v}\right)_\theta = \overrightarrow{u_\theta}.\left(\overrightarrow{\nabla}\times\overrightarrow{v_\perp}\right). \tag{3}$$

Considering these notations, axisymmetric Navier-Stokes equations can be written as a non-dimensional set of three differential equations with forcing terms and homogeneous boundary conditions specified in the following section:

$$E^2(v_\theta) = Re\left\{\overrightarrow{\nabla}\times\left(v_\theta\overrightarrow{u_\theta}\right)\times\left[\overrightarrow{\nabla}\times\psi\overrightarrow{u_\theta}\right]\right\}.\overrightarrow{u_\theta}, \tag{4}$$

$$E^2(\omega) = Re\overrightarrow{\nabla}\times\left\{\left(\overrightarrow{\nabla}\times\overrightarrow{v_\theta}\right)\times\overrightarrow{v_\theta} + \omega\overrightarrow{u_\theta}\times\left[\overrightarrow{\nabla}\times\psi\overrightarrow{u_\theta}\right]\right\}.\overrightarrow{u_\theta}, \tag{5}$$

---

[1] Note that ψ is actually the azimuthal component of the stream vector potential to be considered for the study of 3D flows with the most classical non-primitive formulation of the incompressible Navier-Stokes equation.

$$E^2(\psi) = -\omega. \tag{6}$$

Here, use is made of the differential operator, $E^2()$, defined as:

$$E^2() = \frac{\partial^2()}{\partial z^2} + \frac{\partial^2()}{\partial r^2} + \frac{1}{r}\frac{\partial()}{\partial r} - \frac{()}{r^2}. \tag{7}$$

The two last terms are representative of the curvature effects which are never negligible but more and more pronounced when switching from an annulus to a full cylinder ($r_i \to 0$). A straightforward scaling[2] of the generic operator (7) reveals that the curvature effects are no longer significant when $(r_o - r_i)/r_i \to 0$. Hence, two aspect ratios are sufficient in describing the geometry: the horizontal aspect ratio, $\frac{r_i}{r_o}$, and the vertical aspect ratio, $\frac{h}{r_o}$, with h, the depth of the liquid bath.

B. Boundary conditions as written in terms of mixed variables

Since the inner and outer side walls are maintained stationary while the floor is rotating, no-slip boundary conditions for the azimuthal component of the velocity field,

$$v_\theta = 0 \quad \text{at} \quad r = \frac{r_i}{r_o} \quad \text{along} \quad 0 < z \leqslant \frac{h}{r_o}, \tag{8}$$

$$v_\theta = 0 \quad \text{at} \quad r = 1 \quad \text{along} \quad 0 < z \leqslant \frac{h}{r_o}, \tag{9}$$

$$v_\theta = r \quad \text{at} \quad z = 0 \quad \text{along} \quad \frac{r_i}{r_o} < r < 1, \tag{10}$$

as well as for the radial and vertical components, v_r and v_z,

$$\frac{\partial \psi}{\partial r} = 0 \quad \text{at} \quad r = \frac{r_i}{r_o} \quad \text{along} \quad 0 < z \leqslant \frac{h}{r_o}, \tag{11}$$

$$\frac{\partial \psi}{\partial r} = 0 \quad \text{at} \quad r = 1 \quad \text{along} \quad 0 < z \leqslant \frac{h}{r_o}, \tag{12}$$

$$\frac{\partial \psi}{\partial z} = 0 \quad \text{at} \quad z = 0 \quad \text{along} \quad \frac{r_i}{r_o} < r < 1, \tag{13}$$

together with the impermeability boundary conditions for v_r and v_z,

$$\psi = 0 \quad \text{at} \quad r = \frac{r_i}{r_o} \quad \text{along} \quad 0 < z \leqslant \frac{h}{r_o}, \tag{14}$$

$$\psi = 0 \quad \text{at} \quad r = 1 \quad \text{along} \quad 0 < z \leqslant \frac{h}{r_o}, \tag{15}$$

$$\psi = 0 \quad \text{at} \quad z = 0 \quad \text{along} \quad \frac{r_i}{r_o} < r < 1, \tag{16}$$

are written in terms of the primitive variable, v_θ, and the stream function as well.

On the free liquid surface, the impermeability boundary condition implies that

$$\psi = 0 \quad \text{at} \quad z = \frac{h}{r_o} \quad \text{along} \quad \frac{r_i}{r_o} < r < 1, \tag{17}$$

while the tangential component of the jump momentum balance leads to:

$$\frac{\partial v_r}{\partial z} = 0 \quad \text{at} \quad z = \frac{h}{r_o} \quad \text{along} \quad \frac{r_i}{r_o} < r < 1, \tag{18}$$

$$\frac{\partial v_\theta}{\partial z} = 0 \quad \text{at} \quad z = \frac{h}{r_o} \quad \text{along} \quad \frac{r_i}{r_o} < r < 1. \tag{19}$$

---

[2] cartesian terms: $\frac{\partial}{\partial z^2} \sim \frac{1}{h^2}$ and $\frac{\partial}{\partial r^2} \sim \frac{1}{(r_o - r_i)^2}$

curvature terms: $\frac{\partial}{r \partial r} \sim \frac{1}{r_i (r_o - r_i)}$ and $\frac{1}{r^2} \sim \frac{1}{r_i^2}$.

Finally, considering that the impermeability boundary condition, $v_z = 0$, is uniform along the liquid surface, which means that $\frac{\partial v_z}{\partial r} = 0$, the previous boundary condition (18) can be turned into a Dirichlet condition for the non-primitive variable, ω :

$$\omega = \frac{\partial v_r}{\partial z} - \frac{\partial v_z}{\partial r} = 0 \quad \text{at} \quad z = \frac{h}{r_o} \quad \text{along} \quad \frac{r_i}{r_o} < r < 1. \tag{20}$$

This last boundary condition must be revised in case of uniform contamination along the liquid surface (appendix A).

C. Solutions for the $v_\theta-$, $\omega-$, $\psi-$ problems

Forcing terms of equations (4) – (5) are obviously non-linear. Taking advantage of the slow rotation speed of the floor and of the weak coupling between unknowns, they can be linearized by means of a regular perturbation expansion where Re is a small parameter, leading to an infinite set of linear problems [23, 24]. More specifically, if ζ denotes either v_θ, or ψ or ω, the general solution of the flow can be assumed to be:

$$\zeta = \zeta_0 + Re\zeta_1 + Re^2\zeta_2 + \mathcal{O}(Re^3).$$

From a comparison with available results obtained from both DNS [16] and experiments [25], present analytical calculations can be limited to second-order $\mathcal{O}(Re^2)$, as will be discussed later on in this paper.

The mathematical model (4) – (6) shows that the azimuthal flow field, v_θ, as well as the stream function, ψ, and the vorticity, ω, are all driven by the generic differential operator E^2 but with different forcing terms. An alternative form of E^2 is also writen as,

$$E^2\left(\right) = \frac{\partial^2\left(\right)}{\partial z^2} + E_r^2\left(\right), \tag{21}$$

suggesting at least one eigenvalue problem along the radial coordinate and a second one along the vertical coordinate. Finally, because of the different boundary conditions considered here, three eigenvalue problems can be derived from the model (4) – (6), all of them defined over the open domain $D = \left]\frac{r_i}{r_o}, 1\right[\times \left]0, \frac{h}{r_o}\right[$.

- A first eigenvalue problem along the $r-$axis,

$$E_r^2\left(f\right) = -\beta^2 f, \quad \text{with} \quad \frac{r_i}{r_o} < r < 1, \tag{22}$$

  is common to all three variables, v_θ, ω and ψ, and must be associated with following Dirichlet boundary conditions:

$$f\left(\frac{r_i}{r_o}\right) = 0, \tag{23}$$

$$f(1) = 0. \tag{24}$$

  This leads to an infinite set of orthogonal eigenfunctions, $\{f_j\}$, defined by,

$$f_j\left(r\right) = \left\{\sqrt{\frac{\pi^2\beta_j^2}{2}\frac{J_1^2(\beta_j\frac{r_i}{r_o})}{J_1^2(\beta_j\frac{r_i}{r_o}) - J_1^2(\beta_j)}}\right\} \tag{25}$$
$$.[J_1(\beta_j r)Y_1(\beta_j) - J_1(\beta_j)Y_1(\beta_j r)],$$

  with $j \in \mathbb{N}^*$ and where $J_1\left(\right)$ and $Y_1\left(\right)$ are Bessel functions of the first and second kinds at first order.

  Eigenvalues β_j are given as solutions of the transcendental equation,

$$J_1\left(\beta_j\right)Y_1\left(\beta_j\frac{r_i}{r_o}\right) - J_1\left(\beta_j\frac{r_i}{r_o}\right)Y_1\left(\beta_j\right) = 0.$$

- A second eigenvalue problem along the $z-$axis only for the stream function ψ and the vorticity ω can be written as:

  $$\frac{\partial^2 g}{\partial z^2} = -\alpha^2 g, \quad \text{with} \quad 0 < z < \frac{h}{r_o},$$

  associated with following Dirichlet boundary conditions: $g\left(0\right) = 0$ and $g\left(\frac{h}{r_o}\right) = 0$.

  This leads to a second infinite set of orthogonal eigenfunctions, $\{g_k\}$, defined by:

  $$g_k\left(z\right) = \sqrt{\frac{2r_o}{h}} \sin\left(\alpha_k z\right), \quad \alpha_k = \frac{k\pi r_o}{h} \quad (k \in \mathbb{N}^*).$$

- Finally, a third eigenvalue problem along the $z-$axis devoted to the azimuthal flow field v_θ is written as,

  $$\frac{\partial^2 q}{\partial z^2} = -\gamma^2 q, \quad \text{with} \quad 0 < z < \frac{h}{r_o},$$

  associated with Dirichlet and Neumann boundary conditions,

  $$q\left(0\right) = 0, \tag{26}$$

  $$\left.\frac{\partial q}{\partial z}\right|_{z=\frac{h}{r_o}} = 0. \tag{27}$$

  This leads to a last infinite set of orthogonal eigenfunctions, $\{q_k\}$, defined by

  $$q_k\left(z\right) = \sqrt{\frac{2r_o}{h}} \sin\left(\gamma_k z\right), \tag{28}$$

  with $\gamma_k = \dfrac{(2k-1)\pi r_o}{2h} \quad (k \in \mathbb{N}^*)$.

The solution for the entire flow field is derived from these three sets of orthogonal functions and, considering one particular i^{th}-order, is expanded for each component in double series as

$$v_{\theta,i}\left(r,z\right) = \sum_{k=1}^{+\infty}\sum_{j=1}^{+\infty} v_{\theta,i_{kj}} f_j\left(r\right) q_k\left(z\right), \tag{29}$$

$$\psi_i\left(r,z\right) = \sum_{k=1}^{+\infty}\sum_{j=1}^{+\infty} \psi_{i_{kj}} f_j\left(r\right) g_k\left(z\right), \tag{30}$$

$$\omega_i\left(r,z\right) = \sum_{k=1}^{+\infty}\sum_{j=1}^{+\infty} \omega_{i_{kj}} f_j\left(r\right) g_k\left(z\right), \tag{31}$$

where Fourier coefficients $v_{\theta,i,kj}$ and $\psi_{i,kj}$ are directly calculated by means of the following dot products along the $r-$axis and $z-$axis:

$$\langle u, v\rangle_r = \int_{\frac{r_i}{r_o}}^{1} r u(r) v(r) dr, \tag{32}$$

$$\langle u, v\rangle_z = \int_0^{\frac{h}{r_o}} u(z) v(z) dz. \tag{33}$$

D. On the use of the integral vorticity condition

A look at boundary conditions (14) – (17) and (20) shows that ψ-conditions are overspecified along the edge of the D-domain at the expense of ω conditions. According to Quartapelle *et al.* [26], these boundary conditions in-excess for the stream function can be redistributed on the vorticity as follows: the $\omega_{i,kj}$ coefficients are implicitly calculated by making use of the second Green's identity written here with the E^2 operator as:

$$\int_D \left(\psi E^2\left(\Phi\right) - \Phi E^2\left(\psi\right)\right) dA = \int_{\partial D} \left(\psi \frac{\partial \Phi}{\partial n} - \Phi \frac{\partial \psi}{\partial n}\right) dl,$$

where $\frac{\partial}{\partial n}$ is the normal derivative to the edge ∂D which delimits the D-domain, and Φ is an arbitrary scalar field.

The Φ scalar field can be constrained here in such a way that $E^2\left(\Phi\right) = 0$ throughout the D-domain. This leads to a new formulation of the Green's identity, referred to here as the integral condition for the vorticity:

$$\int_D r\Phi\left(r,z\right)\omega\left(r,z\right) dA = -\int_{\frac{r_i}{r_o}}^{1} r\Phi\left(r,\frac{h}{r_o}\right)\frac{\partial \psi}{\partial z}\left(r,\frac{h}{r_o}\right) dr. \tag{34}$$

Hence, the three boundary conditions (11)-(13) can be reassigned to the vorticity ω. It must be noticed that the eigenfunctions $f_j\left(r\right)$ and $g_k\left(z\right)$ have been built considering homogeneous Dirichlet boundary conditions which are not checked for ω anywhere but at the interface. Yet the ω-solution is assumed to converge on the entire D-domain excluding boundaries where the proposed solution naturally vanishes. Incidentally, close to the side walls and to the floor where boundary conditions are unknown, ω can fulfill a Dirichlet boundary condition leading to:

$$\lim_{z\to 0}\omega\left(r,z\right) = \omega^f\left(r\right) = \sum_{j=1}^{+\infty}\omega_j^f f_j\left(r\right), \tag{35}$$

$$\lim_{r\to \frac{r_i}{r_o}}\omega\left(r,z\right) = \omega^i\left(z\right) = \sum_{k=1}^{+\infty}\omega_k^i g_k\left(z\right), \tag{36}$$

$$\lim_{r\to 1}\omega\left(r,z\right) = \omega^o\left(z\right) = \sum_{k=1}^{+\infty}\omega_k^o g_k\left(z\right), \tag{37}$$

where ω_j^f, ω_k^i and ω_k^o sequences, while assumed to be known, are used for the general solution of the problem though they are calculated in a second step (see details in appendix B for their calculation at $\mathcal{O}(\mathrm{Re})$). By combining this last assumption with the second Green's identity, the difficulty related to inappropriate boundary condition distribution can be overcome.

To our knowledge, this treatment based on an integral boundary condition is original.

E. Solution of the problem

The $v_\theta-$, $\omega-$ and $\psi-$ solutions are determined using the general method presented in section II C. Considering the unknowns v_θ, ω and ψ, the problem presents a welcome property: it can be demonstrated that the azimuthal flow field vanishes at odd orders (*i.e.* $v_{\theta,1} = 0$, $v_{\theta,3} = 0$, etc...) while the stream function ψ and the vorticity ω vanish at even orders (*i.e.* $\psi_0 = \omega_0 = 0$, $\psi_2 = \omega_2 = 0$, etc...):

$$v_\theta(r,z) = v_{\theta,0}(r,z) + Re^2\ v_{\theta,2}(r,z) + \mathcal{O}(Re^4), \tag{38}$$

$$\psi(r,z) = Re\ \psi_1(r,z) + \mathcal{O}(Re^3), \tag{39}$$

$$\omega(r,z) = Re\ \omega_1(r,z) + \mathcal{O}(Re^3). \tag{40}$$

As a result, the azimuthal and meridian flow fields are solved alternatively by forcing terms dependent on previously calculated orders, with a consequent reduction in the number of solutions to calculate. This also highlights the axisymmetric geometry of the swirling flow which is characterized by a weak coupling between the 1-D annular flow along the azimuthal direction and the 2-D recirculating flow within a meridian cross-section of the channel.

1. Solution at zeroth-order

As mentioned above, the model to solve at zeroth-order ($\omega_0 = \psi_0 = 0$) is written as:

$$E^2\left(v_{\theta,0}\right) = 0,$$

with the boundary conditions (8) – (10) and (19) must be associated. This corresponds to the Stokes solution for the azimuthal flow.

From the contents of section II C, by making use of the second Green's identity when projecting relevant (orthogonal) eigenfunctions on the E^2-operator, the solution can be expanded according to the double series:

$$v_{\theta,0}(r,z) = \frac{2r_o}{h}\sum_{j=1}^{+\infty}\Bigg[\left(\sum_{k=1}^{+\infty}\frac{\gamma_k}{\gamma_k^2+\beta_j^2}\sin\left(\gamma_k z\right)\right) . \left\langle v_\theta(r,z=0), f_j\right\rangle_r f_j(r)\Bigg], \tag{41}$$

with $v_\theta(r, z = 0) = r$ (see e.g. (A5) with $Z_{k_j}(v_\theta,\omega,\psi) = \mathrm{Bo} = 0$). Referring to [27], this can be simplified into the single series:

$$v_{\theta,0}\left(r,z\right) = \sum_{j=1}^{+\infty} v_{\theta,0_j}\, x_j\left(z\right) f_j\left(r\right), \tag{42}$$

with $v_{\theta,0_j} = \left\langle r, f_j\right\rangle_r$ and where $x_j\left(z\right)$ writes:

$$x_j\left(z\right) = \left[\frac{2\sinh\left[\beta_j\left(\frac{2h}{r_0}-z\right)\right]}{\sinh\left(\frac{2h}{r_0}\beta_j\right)} - \frac{\sinh\left[\beta_j\left(\frac{h}{r_0}-z\right)\right]}{\sinh\left(\frac{h}{r_0}\beta_j\right)}\right].$$

Such a solution is quite similar to but simpler than those developed by Mannheimer and Schechter [25] and Pintar *et al.* [28] in the very first analytical studies of this complex flow. Although we used trigonometric series which best fit closed geometries along the z-axis, the latter ones asymptotically converge to the same hyperbolic lines for the particular case of a free surface.

Finally, as illustrated here, and anticipating on what follows, all the analytical solutions for the flow are calculated from the second Green's identity and dot products between unknown variables and eigenfunctions. This is worthy of note since it allows us to process the corner singularities at the bottom of the channel with no risk of divergence.

2. Solution at first-order

The weak coupling between azimuthal and meridian flows can be highlighted in the problem at the N^{th}-order by the presence of a source term which depends on solutions calculated at lower n^{th}-orders (n < N).

Since the azimuthal flow vanishes at first-order, the vorticity ω_1 is given as the solution of the inhomogeneous equation:

$$E^2(\omega_1) = V(v_{\theta,0}; v_{\theta,0}), \tag{43}$$

with

$$V(u;v) = \left[\overrightarrow{\nabla}\times\left(\overrightarrow{\nabla}\times u\overrightarrow{u_\theta}\right)\times v\overrightarrow{u_\theta}\right].\overrightarrow{u_\theta}.$$

Use of the interfacial boundary condition (20) and the boundary expansions (35) – (37) leads after some calculations [29] to:

$$\omega_1(r,z) = \sum_{j=1}^{+\infty}\sum_{k=1}^{+\infty}\omega_{1,kj}(r,z) f_j(r) g_k(z), \tag{44}$$

$$\text{with}\quad \omega_{1,kj}(r,z)=\sum_{j=1}^{+\infty}\sum_{k=1}^{+\infty}\left\{\frac{1}{\alpha_k^2+\beta_j^2}\left[h_{kj}+\sqrt{\frac{2r_o}{h}}\alpha_k\overset{f}{\omega}_{1,j}+\overset{i}{\omega}_{1,k}\left.\frac{\partial f_j}{\partial r}\right|_{\frac{r_i}{r_o}}-\overset{o}{\omega}_{1,k}\left.\frac{\partial f_j}{\partial r}\right|_{1}\right]\right\},$$

$$\text{where}\quad h_{kj}=-2\int_{\frac{r_i}{r_o}}^{1}\int_{0}^{\frac{h}{r_o}}v_{\theta,0}^2\left(r,z\right)f_j\left(r\right)\frac{\partial g_k\left(z\right)}{\partial z}drdz,$$

$$=-2\sum_{m=1}^{+\infty}\sum_{n=1}^{+\infty}v_{\theta,0_m}v_{\theta,0_n}\left(\int_{0}^{\frac{h}{r_0}}x_m\left(z\right)x_n\left(z\right)\frac{\partial g_k\left(z\right)}{\partial z}dz\right)\left(\int_{\frac{r_i}{r_o}}^{1}f_m\left(r\right)f_n\left(r\right)f_j\left(r\right)dr\right).$$

Note that use is made of (42) to find the last expression for the coefficient h_{kj}.

Finally considering the third differential problem,

$$E^2\left(\psi_1\right)=-\omega_1,$$

the expression of $\psi_1(r,z)$ is similar to that of $\omega_1(r,z)$ in (44), $\psi_1(r,z)=\sum\limits_{j=1}^{+\infty}\sum\limits_{k=1}^{+\infty}\psi_{1,kj}(r,z)f_j(r)g_k(z)$, but its coefficients are written as:

$$\psi_{1_{kj}}(r,z)=\frac{\omega_{1,kj}(r,z)}{\alpha_k^2+\beta_j^2}. \tag{45}$$

3. Solution at second-order

Only azimuthal flow field is involved at this even order when we solve the following problem:

$$E^2\left(v_{\theta,2}\right)=U\left(v_{\theta,0};\psi_1\right), \tag{46}$$

with

$$U(u;v)=\left[\overrightarrow{\nabla}\times u\overrightarrow{u_\theta}\times\left(\overrightarrow{\nabla}\times v\overrightarrow{u_\theta}\right)\right].\overrightarrow{u_\theta},$$

and the four associated boundary conditions:

$$\begin{aligned}&\text{along}\quad 0<z\leqslant\frac{h}{r_o}:\\&\qquad v_{\theta,2}=0\quad\text{at}\quad r=(1,\frac{r_i}{r_o}),\\&\text{along}\quad \frac{r_i}{r_o}<r<1:\\&\qquad v_{\theta,2}=0\quad\text{at}\quad z=0,\\&\qquad \frac{\partial v_{\theta,2}}{\partial z}=0\quad\text{at}\quad z=\frac{h}{r_o}.\end{aligned}$$

It is not straightforward to find the solution to this problem which can be written as,

$$v_{\theta,2}(r,z)=-\sum_{k=1}^{+\infty}\sum_{j=1}^{+\infty}\frac{1}{\beta_j^2+\gamma_k^2}U_{kj}\left(v_{\theta,0},\psi_1\right)q_k\left(z\right)f_j\left(r\right), \tag{47}$$

where

$$
\begin{aligned}
U_{kj}\left(v_{\theta,0},\psi_1\right) &= \left\langle \left\langle U\left(v_{\theta,0},\psi_1\right), q_k\right\rangle_z, f_j\right\rangle_r \\
&= -\int\limits_{\frac{r_i}{r_o}}^{1}\int\limits_{0}^{\frac{h}{r_0}} r^2 v_{\theta,0}\left(r,z\right)\left[v_{r,1}\left(r,z\right)\frac{\partial f_j\left(r\right)}{\partial r}q_k\left(z\right)+v_{z,1}\left(r,z\right)\frac{\partial q_k\left(z\right)}{\partial z}f_j\left(r\right)\right]drdz \\
&= -\sum_{l,m,n=1}^{+\infty} v_{\theta,0_l}v_{r,1_{mn}}\left(\int\limits_{\frac{r_i}{r_o}}^{1} r^2 f_l\left(r\right)f_m\left(r\right)\frac{\partial f_j\left(r\right)}{\partial r}dr\right)\left(\int\limits_{0}^{\frac{h}{r_o}} x_l\left(z\right)g_n\left(z\right)q_k\left(z\right)dr\right) \\
&\quad -\sum_{l,m,n=1}^{+\infty} v_{\theta,0_l}v_{r,1_{mn}}\left(\int\limits_{\frac{r_i}{r_o}}^{1} r^2 f_l\left(r\right)f_m\left(r\right)f_j\left(r\right)dr\right)\left(\int\limits_{0}^{\frac{h}{r_o}} x_l\left(z\right)g_n\left(z\right)\frac{\partial q_k\left(z\right)}{\partial z}dr\right). \qquad (48)
\end{aligned}
$$

III. RESULTS AND DISCUSSION

A. Azimuthal flow field

As contribution at leading order to the azimuthal flow field is expressed as a single series, the rate of convergence of the series solution (42) is first studied. Due to corner singularities for velocity at the edges of the rotating disk, related to the non-physical jump in the Dirichlet boundary conditions for the velocity, the series solution needs to be approximated with a truncation number near the floor much larger than that required for finding the velocity along the liquid surface [21]. Corner singularities stand as a topic extensively addressed by many authors in the literature devoted to numerical issues (see e.g. [30, 31]). In this case, our aim is to find an analytical solution without resorting to the use of a local analytical solution [32, 33] or to Lanczos factors for accelerating convergence of the series [11]. Fortunately, in the present situation of an end-driven annular flow, the gap between the rotating floor and the stationary side walls is the natural length scale allowing the corner singularities to be processed. Because one fundamental aim of the present paper is to develop an analytical formulation with no compromise with the physical situation, a linear velocity profile is prescribed as a relaxed boundary condition across a non-dimensional gap width, s:

$$
\begin{aligned}
&v_\theta(r,z) = \frac{\left(r-\frac{r_i}{r_o}\right)\left(\frac{r_i}{r_o}+s\right)}{s} \\
&\quad \text{for} \quad \frac{r_i}{r_o} < r < \left(\frac{r_i}{r_o}+s\right) \quad \text{and} \quad z=0, \qquad (49) \\
&v_\theta(r,z) = r \\
&\quad \text{for} \quad \left(\frac{r_i}{r_o}+s\right) \leqslant r \leqslant (1-s) \quad \text{and} \quad z=0, \qquad (50) \\
&v_\theta(r,z) = \frac{(1-r)(1-s)}{s} \\
&\quad \text{for} \quad (1-s) < r < 1 \quad \text{and} \quad z=0. \qquad (51)
\end{aligned}
$$

Here, the jump in the swirl velocity v_θ is replaced by a jump in $\frac{\partial v_\theta}{\partial r}$ and doing this, the linear Couette profile so imposed along the gap is thought of as physically relevant to model the conditions of lubrication between the side walls and the rotating floor. Note that an alternative approach to treat the corner singularities is proposed by Lopez and Chen, which consists in using a boundary layer function [30, 31].

Figure 2 shows the relationship between the vertical distance measured from the rotating floor and the truncation threshold N required so that correction by $(N+1)^{th}$-term is less than $\epsilon = 10^{-3}$ with and without corner singularities and for a reference channel geometry ($r_i/r_o = 0.8$ and $h/r_o = 0.2$). As expected, the convergence rate is faster when the relaxation method based on use of a prescribed profile along the gaps is applied, since no more than 50 terms are necessary to find a solution with target precision near the rotating floor. Note that one term is sufficient to obtain the required level of precision at the vicinity of the liquid surface. The search for an analytical solution to this complex flow, and the mathematical strategy applied here, are enhanced by this significant property. Now, if we consider non-relaxed boundary conditions, the radial profiles of $v_{\theta,0}$ at different depths are reported in Figure 3 for the geometry under consideration and for a truncation threshold based on the first 200 terms. As expected, while the radial profiles are close to a parabolic shape near the air/water interface, they become more linear near the bottom of the channel due to the linear distribution of momentum imposed by the no-slip boundary condition. Still in Figure 3, it is also worthy to note that the reducing of the velocity scale with the vertical elevation ($v_{\theta,0} \sim 1$ at $z \sim 0.01\dfrac{h}{r_o}$ while $v_{\theta,0} \sim 0.1$ at $z \sim \dfrac{h}{r_o}$) is well explained by the conservation of the axial angular momentum, $\dfrac{d[r\ v_\theta]}{dt} = 0$, in the control volume defined as $[0..z] \times [r_i..r_o]$. As a matter of fact, the source of angular momentum, typically the viscous torque along the rotating end wall, is balanced by the resisting viscous torques along the inner and outer side walls.

Introduction of smoothing boundary conditions (49 -51) is expected to modify these $v_{\theta,0}$ profiles. Consequently, as demonstrated by equation (43), we also expect gap size, s, to have an impact on the meridian flow pattern, which solely depends on $v_{\theta,0}(r,z)$. As illustrated in Figure 3, the azimuthal profiles would appear to be sensitive to a growing value of s only at the vicinity of the inner and outer corners where smoothing conditions (49 -51) apply. However, the s gap impact on azimuthal profiles in this area rapidly vanishes when it moves away from the rotating end floor as illustrated in Figure 4. This is confirmed by a detailed inspection of the indicator, $R_s = \dfrac{v_{\theta,0}(r,z,s)}{v_{\theta,0}(r,z,s=0)}$, introduced to quantify deviation from the non-relaxed case as a function of s parameter; R_s is therefore defined as the ratio between two azimuthal velocities at leading order: a first one calculated with the linear profile along the gap s, $v_{\theta,0}(r,z,s)$, and the second one, $v_{\theta,0}(r,z,s=0)$, calculated with a jump in the velocity at the corners. Minimum and maximum values of R_s are determined all along the profiles for various s values. Table I shows that, with smoothing boundary conditions, significant discrepancies in $v_{\theta,0}(r,z)$ only occur at the very vicinity of the rotating wall ($z < 0.1h/r_o$). The no-gap case is also sometimes overshot by a solution with a smoothed boundary condition ($z = 0.01h/r_o$ and $s > 0.01$) in the neighborhood of the corner singularities (results not shown here). To maintain a regular behavior of $v_{\theta,0}$, a very low value of $s = 0.004$ has been often chosen hereafter in this paper, thus ensuring a more physical picture of existing annular flow devices (see e.g. [15]).

Table I. Evaluation of maximum/minimum values of the parameter R_s along the velocity profiles for different values of both the channel depth $z/(h/r_o)$ and the gap s (horizontal and vertical aspect ratios: $\frac{r_i}{r_o}$ =0.8 and $\frac{h}{r_o}$ =0.2). Truncation threshold of the $v_{\theta,0}(r,z)$ series is set to 200 terms.

	R_s									
	$s = 0.001$		$s = 0.002$		$s = 0.004$		$s = 0.008$		$s = 0.01$	
$z/(h/r_o)$	Min	Max	Min	Max	Min	Max	Min	Max	Min	Max
0.01	0.9373	1.0471	0.8040	1.1813	0.5709	1.5003	0.3411	1.2984	0.2821	1.2431
0.1	0.9991	1.0000	0.9965	1.0000	0.9863	0.9998	0.9486	0.9994	0.9233	0.9990
0.2	0.9998	1.0000	0.9990	0.9999	0.9962	0.9997	0.9851	0.9988	0.9770	0.9980
0.5	0.9999	1.0000	0.9998	0.9999	0.9990	0.9994	0.9961	0.9976	0.9940	0.9963
1	1.0000	1.0000	0.9998	0.9998	0.9993	0.9993	0.9972	0.9974	0.9957	0.9959

Table II. Evaluation of the second-order correction to the maximum magnitude and related location of surface azimuthal velocity v_θ as a function of vertical aspect ratio ($Re = 100$ and $r_i/r_o = 0.8$).

	Order 0		**Order 2**		**Relative deviation**	
h/r_o	Position	Magnitude	Position	Magnitude	Position	Magnitude
0.3	0.897858522	0.0204196	0.897950995	0.0204054	0.01 %	0.07 %
0.2	0.898206786	0.098269	0.898152027	0.0982326	0.01 %	0.04 %
0.1	0.899955455	0.44899	0.899517549	0.44888	0.05 %	0.02 %
0.06	0.903311568	0.73389	0.903089666	0.73373	0.02 %	0.02 %

Table III. Sensitivity to Reynolds number, Re, of the impact of the second-order correction upon the maximum magnitude and related location of surface azimuthal velocity v_θ (aspect ratios: $r_i/r_o = 0.8$ and $h/r_o = 0.2$).

Re	Max. location	Relative deviation	Max. magnitude	Relative deviation
0	0.898206953	–	0.0982684	–
10	0.898206232	8.10^{-5} %	0.0982702	0.002 %
100	0.898153074	0.006 %	0.0982424	-0.026 %
200	0.897991332	0.024 %	0.0981466	-0.124 %

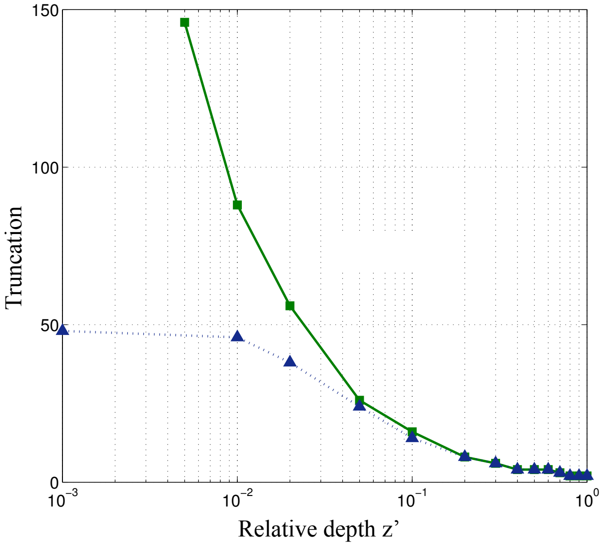

Figure 2. (color online) Truncation threshold N required to achieve an absolute precision better than $\epsilon = 10^{-3}$ on the calculated azimuthal velocity at leading order, $v_{\theta,0}(r, h/r_o)$, as a function of the normalized distance from the rotating floor $z = z'h/r_o$, with (▲, s=0.004) and without (■, s=0) relaxed boundary conditions at the corners.

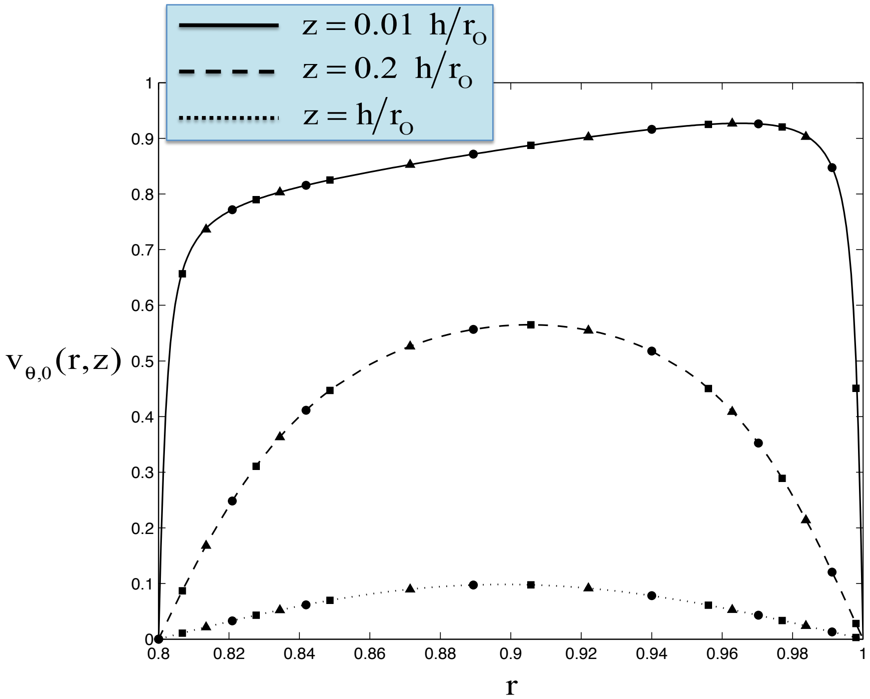

Figure 3. Azimuthal velocity profiles at leading order $v_{\theta,0}(r, z)$ as a function of the normalized distances, r and z where $s = 0$ and geometrical aspect ratios $r_i/r_o = 0.8$ and $h/r_o = 0.2$ (line curves). Comparison with profiles computed with boundary conditions relaxed by gap conditions (● $s = 0.001$, ■ $s = 0.002$ and ▲ $s = 0.004$).

Finally, as shown by the regular perturbation (38), the azimuthal flow at leading order can be corrected by the solution at second-order (47). By anticipating on the following and assuming that the solution of equation (43) discussed in subsection III B is available, table II shows that the correction at second-order is not really significant for a reference horizontal aspect ratio ($r_i/r_o = 0.8$) and different vertical aspect ratios h/r_o ranging from 0.06 to 0.3. Position and magnitude of the maximum values of velocity profiles along the liquid surface are compared with and without the second-order correction at $Re = 100$. Maximum relative deviations are less than 0.05% and 0.07% for

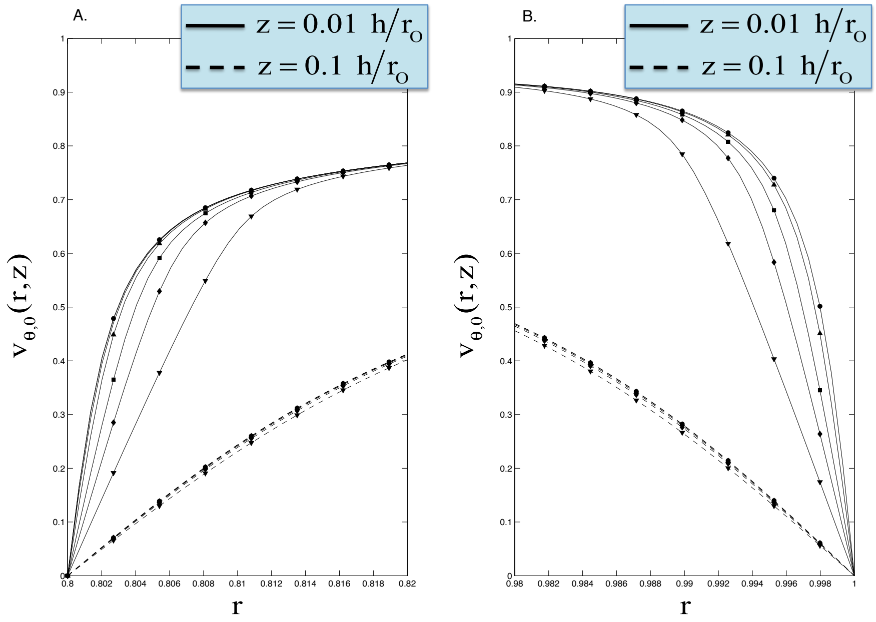

Figure 4. Sensitivity of azimuthal velocity profiles at leading order $v_{\theta,0}(r,z)$ to the s gap relaxation parameter for two different depths ($z = 0.01h/ro$ and $z = 0.1h/ro$): (●) $s = 0$, (▲) $s = 0.002$,(■) $s = 0.004$, (◆) $s = 0.006$ and (▼) $s = 0.01$. A. Near the inner side wall ($r \sim \frac{r_i}{r_o}$). B. Near the outer side wall ($r \sim 1$). Geometry: $r_i/r_o = 0.8$ and $h/r_o = 0.2$.

both indicators respectively. Keeping the same horizontal aspect ratio, $r_i/r_o = 0.8$, but now considering a typical vertical aspect ratio of $h/r_o = 0.2$, dependence of the azimuthal flow to the correction at second-order is also estimated in Table III when the Reynolds number is made to vary. The relative deviation in azimuthal velocity along the liquid surface appears to be less than 0.124% throughout the range of Re-numbers extending from 0 to 200. Note that this result is confirmed from DNS simulations previously performed by Lopez and Hirsa (here referred to as LH98) using the same base geometry [16].

The azimuthal flow along the liquid surface as analytically calculated up to second-order is finally validated by comparison with experimental data from Manheimer and Schechter [25] and with DNS calculations from LH98 [16], both of which are obtained with the same geometrical aspect ratios ($h/r_o = 0.13$ and $r_i/r_o = 0.8$) at $Re = 146$. Results are illustrated in Figure 5. Note that our model tends to slightly underestimate experimental values while DNS calculations tend to slightly overestimate them.

B. Meridian flow field

The first-order solution of equation (43) gives the stream function $\psi_1(r,z)$, using the relationship (45) between stream function and vorticity coefficients obtained as a projection of the differential equation (II E 2) on the eigenfunctions f_j and g_k. Solutions $\omega_1(r,z)$ and $\psi_1(r,z)$ are implicitly validated from the second-order correction analyzed in the previous subsection III A focusing on the azimuthal flow field, $v_\theta(r,z)$. Convergence tests are also performed (not shown here) to demonstrate that the stream function is no longer dependent on the gap s, provided it is small enough.

To determine a channel design which best fits needs for applications involving, for instance, a flow control along the liquid surface at the top of the cavity [7, 15, 34, 35], the influence of geometrical aspect ratios on the meridian flow is investigated. As represented in Fig. 6, the ratio of the maximum radial velocity over the maximum azimuthal velocity, $v_{r_{max}}/v_{\theta_{max}}$, is calculated along the liquid surface for different vertical aspect ratios, $h/r_o \sim [0.06 - 0.3]$, with a unit Reynolds number (Re=1), a horizontal aspect ratio, $r_i/r_o = 0.8$, and a gap, $s = 0.004$. These conditions are the ones of the configuration calculated in LH98 [16] if $h/r_o = 0.2$. Beyond the non monotonic distribution of $v_{r_{max}}/v_{\theta_{max}}$, it is worthy to note that an optimized ratio, $v_{r_{max}}/v_{\theta_{max}} \sim 10^{-3}$, at the liquid surface is achieved for a vertical aspect ratio $h/r_o \sim 0.25$, a value which is surprisingly closed to pioneering configuration of Manheimer & Schechter with $h/r_o = 0.2$ [25]. A second point to notice is that for a vertical aspect ratio $h/r_o = 0.2$, the latter ratio ($v_{r_{max}}/v_{\theta_{max}} \sim 0.92\ 10^{-3}$) is found to be of same order of magnitude as the one found in LH98 ($v_{r_{max}}/v_{\theta_{max}} \sim 0.6\ 10^{-3}$, [16]). Nevertheless, a difference remains between these two values, which suggests that the ratio $v_{r_{max}}/v_{\theta_{max}}$ is highly sensitive to the way

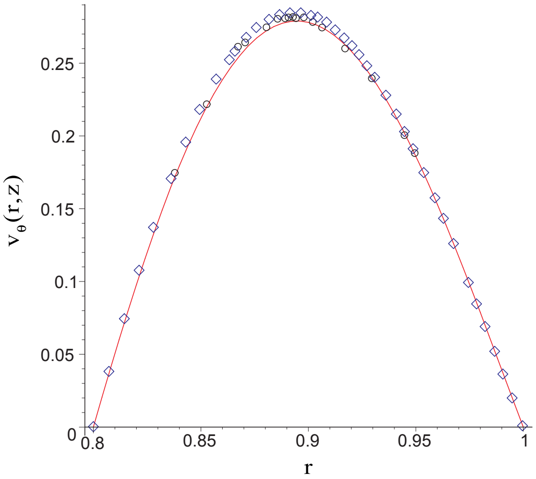

Figure 5. (color online) Comparison along a free liquid surface between (−) the azimuthal velocity profile, as calculated at $\mathcal{O}(Re^2)$ in this paper, $v_{\theta_0}(r, h/r_o) + Re^2 v_{\theta_2}(r, h/r_o)$, (⋄) the azimuthal velocity, $v_\theta(r, h/r_o)$, as calculated from DNS by LH98 [16], and (∘) the velocity as measured by Manheimer and Schechter [25], for the following parameters: $Re = 146$, $r_i/r_o = 0.8$ and $h/r_o = 0.13$, $s = 0.004$).

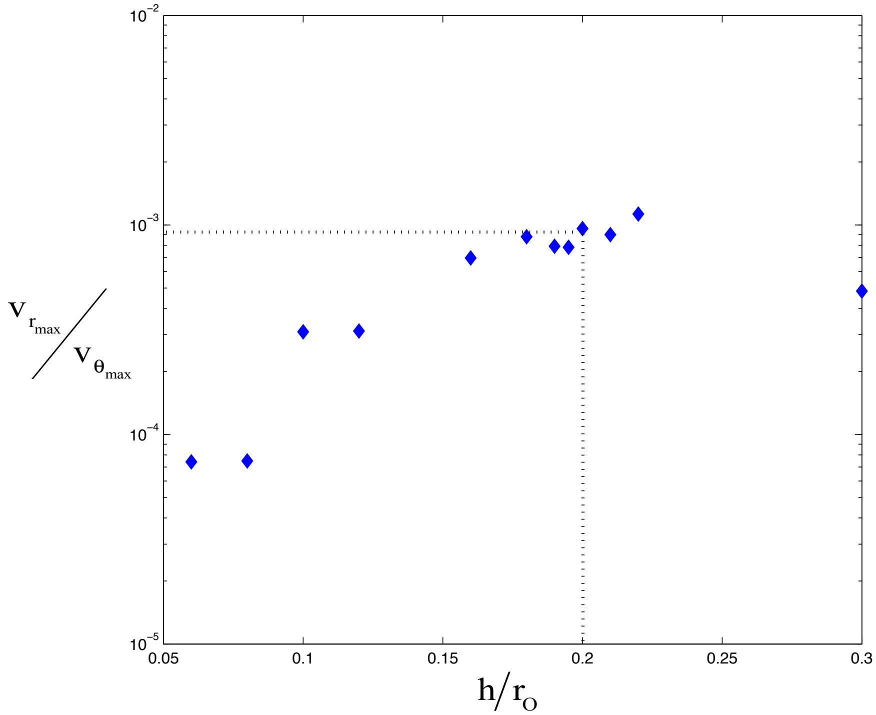

Figure 6. Ratio of maximum radial velocity over maximum azimuthal velocity, $v_{r_{max}}/v_{\theta_{max}}$, along the liquid surface, as a function of vertical aspect ratio for $Re = 1$, $r_i/r_o = 0.8$ and $s = 0.004$. Horizontal and vertical dotted lines are drawn to identify the flow pattern calculated in LH98 [16].

the gap s is processed (see e.g. the impact of the gap upon the profile $v_\theta(r)$: Fig. 4).

1. The weakly non-linear regime

The linear (Stokes) regime is expected in the range: Re ∼ 0 - 250. To estimate the ability of the present model to address the weakly nonlinear regime, a comparison with DNS data extracted from LH98 configuration [16]: $\frac{r_i}{r_o} = 0.8$,

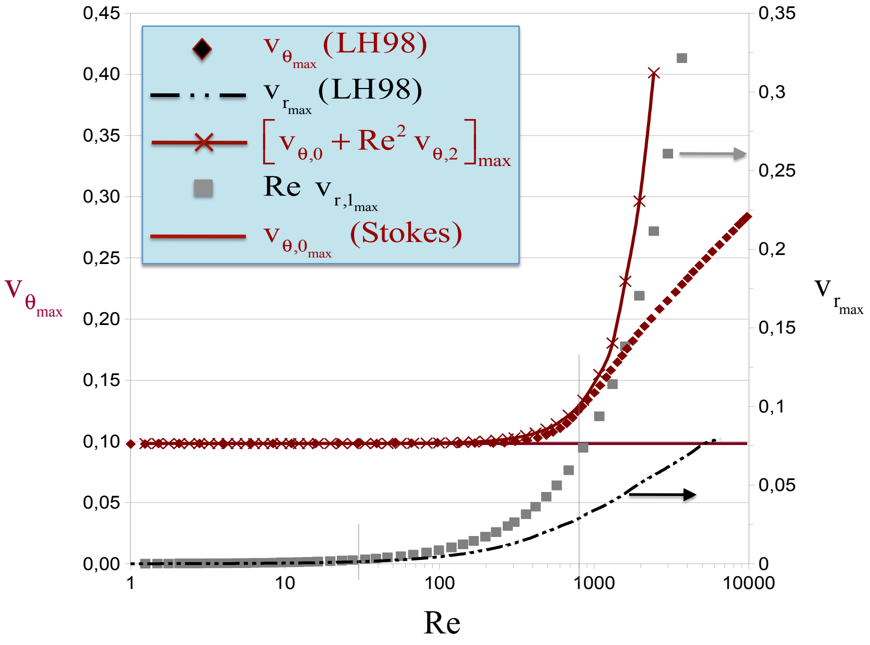

Figure 7. Maximum radial and azimuthal components of the velocity along the liquid surface, $v_{r_{max}}$ (right axis) and $v_{\theta_{max}}$ (left axis), respectively, as a function of the Reynolds number. Comparison between velocities at successive $\mathcal{O}(Re^n)$-orders (n=0, 1, 2) and DNS calculations of LH98 [16] for $\frac{r_i}{r_o} = 0.8$, $\frac{h}{r_o} = 0.2$ and s=0.004.

$\frac{h}{r_o} = 0.2$. The Re-dependence of the maximum values of the radial and azimuthal velocities along the liquid surface is shown in figure (7), namely, the azimuthal (Stokes) flow at zeroth-order, $v_{\theta,0_{max}}$, the radially inward flow as calculated at $\mathcal{O}(Re)$-order, $Re\ v_{r,1_{max}}$, and the azimuthal flow as corrected by the solution at $\mathcal{O}(Re^2)$-order, $v_{\theta,0_{max}} + Re^2\ v_{\theta,2_{max}}$. A first discrepancy between the first-order solution and DNS data can be made evident for Re beyond a critical value, $Re_c \sim 30$. As for the azimuthal flow, the second-order correction is found fruitful since a first significant discrepancy with DNS results is made evident from $Re_c \sim 800$ (to be compared to $Re_c \sim 250$ for the Stokes flow). Higher order corrections are not considered because this paper focuses on the calculation of the (laminar) meridian flow at leading order.

2. *Moffatt eddies*

Contour plots of the stream function $\psi_1(r, z)$ are reported in Figures 8 and 9. Note here that the streamlines are represented as a first-order correction without dependence on the Reynolds number. Nevertheless, based on a previous analysis carried out on sensitivity of the azimuthal flow to the Reynolds number (Tables II – III), observations on the meridian flow can be consistently considered robust even for Re $\sim$ 10.

As the literature leads us to expect, two Moffatt eddies are found in some of our configurations, located at the two lower corners. Whatever the values of the aspect ratios, the vorticity of corner eddies is systematically found to be positive, contrary to what is dictated by centrifugation. A close inspection of figures 8 – 9 shows that small values of the vertical and horizontal aspect ratios enhance the ability of corner discontinuities to behave as a strong localized source of vorticity, especially when the horizontal aspect ratio (radial extent) is small enough (Figs. 9C – 9D). The case of a full cylinder is asymptotically close to our configuration when $\frac{r_i}{r_0} \to 0$. As mentioned in the experimental work by Spohn *et al* [2], the vibrations can change the flow pattern due to the modified gaps between the rotating floor and the stationary side walls. It is therefore not so surprising here to note how the presence or the absence of Moffatt eddies can affect the overall topology of the recirculating flow (Figs 8 – 9).

3. *Influence of the vertical aspect ratio h/r_o*

If channel width is maintained constant (*i.e.* $r_i/r_o = 0.8$), changes in flow patterns with respect to h/r_o are not trivial but whatever the value of the vertical aspect ratio, the flow remains unconditionally radially inward along the liquid surface. It is worthy to note that the aspect ratio h/ro determines the volume of fluid driven by the meridional flow. For a given Re number and a constant horizontal aspect ratio, increasing the vertical aspect ratio h/ro results in a larger volume of fluid being moved and hence a weaker overall meridian flow (Figure 8). This can be explained by the centrifugal force along the rotating end wall which behaves as a source of momentum for the meridian flow. Near a smallest value of the vertical aspect ratio, $h/r_o = 0.06$ (Figure 8.A), the configuration can be seen as particularly flattened: in addition to Moffatt eddies at the corners, a counter-clockwise co-rotating vortex pair with axis along the radial direction becomes evident, embedded in a recirculating core flow whose negative vorticity is induced by centrifugation in the meridian plane. Here, due to the growing importance of curvature effects, the symmetry of the 2-D recirculating flow, $\overrightarrow{v_\perp}$, with respect to the vertical median axis of the cross-section ($r = \frac{r_i}{r_o} + \frac{r_o - r_i}{2\, r_o}$) is demonstrated to be definitely broken for a cylindrical geometry; this can be seen from the values taken by the stream function at the center of the vortices. Such a symmetry is only made possible for the configuration of a straight channel with a moving floor. The presence of the counter-clockwise vortex pair is consistent with a constructive interaction between centrifugation and the secondary vortices induced by viscosity from the Moffatt eddies at the corners.

When the vertical aspect ratio h/r_o is large enough, previous symmetry tends to be recovered (Fig. 8B-D). Also mentioned in the literature on full cylinders, a single cell in the core of the meridian flow with a negative vorticity (see e.g. Fig. 8B for $h/r_o = 0.14$) is not the only flow pattern observed.

For an aspect ratio as large as $h/r_o = 0.19$, a stratified flow pattern made from a vertical stack of two counter-rotating vortical cells is revealed (Fig. 8C). According to eq. (5), the vorticity is generated by a nonlinear forcing term. At $\mathcal{O}(\mathrm{Re})$-order, this forcing term is non linearly dependent on the azimuthal velocity (see eq. 43) and consequently, it is not straightforward to interpret the sign of the vorticity from a vertical dependence of the azimuthal velocity profiles. To explain the stack of two vortical cells with opposite vorticities, it is interesting to consider Hills [10] who demonstrated for a semi-infinite cylinder that a stack of alternate eddies can be present even when inertia is small.

4. Influence of the horizontal aspect ratio r_i/r_o and curvature effects

A constant depth is now considered where $h/r_o = 0.2$. The horizontal aspect ratio, r_i/r_o, is made to decrease ($r_i/r_o = 0.8 \rightarrow 0.1$), while the outer diameter is maintained constant. The consequent enlargement of the annular channel modifies the flow pattern markedly, as demonstrated in Figs. 9A–9D.

Not surprisingly, the vortex of positive vorticity, already evident near the rotating floor in Fig. 8C for $r_i/r_o = 0.8$ and $h/r_o = 0.19$, is again observed in Figure 9A for $r_i/r_o = 0.8$ and $h/r_o = 0.2$. However, for smaller values of the horizontal aspect ratio, $r_i/r_o = 0.6 \rightarrow 0.1$ (Figs. 9B – 9D), it is progressively replaced by two Moffatt eddies arising at lower corners. From these observations, it can be inferred that when $\frac{r_i}{r_o}$ is large enough (small gap: $\frac{r_i}{r_o} \sim \mathcal{O}(1)$):

- the previous symmetry of the 2-D meridian flow with respect to the vertical median axis is recovered, as illustrated by Moffat eddies of same magnitude at the left and right corners and as expected since prescribed azimuthal velocities become asymptotically of same order. This point is clearly checked in Fig. 9B (in contrast with Fig. 9D).

- Moffatt eddies are merging, giving rise to one single cellular pattern of positive vorticity, confined near the rotating floor (Fig. 9A).

When the cavity is stretched more horizontally (small value of r_i/r_o), the growing influence of curvature effects, as revealed from previous break-up of symmetry within the cross-section, is again observed: the point of maximum vorticity in the core flow moves radially outward from the middle axis of the cavity. This is the result of the linear increase of centrifugation along the radial direction. As observed in Figs. 9C – 9D, the latter symmetry break-up is also demonstrated by the values of the stream function at corner singularities. As expected, due to a large jump in the boundary conditions for velocity at the right corner, the Moffatt vortex induced by viscosity significantly perturbs the main flow.

Although both the radial and vertical aspect ratios, r_i/r_o and h/r_o, have a significant effect on the flow pattern, they do not have the same effect: the enhancement of curvature effects as induced by radially inward enlargement of the channel does not drive the presence of two stacked counter-rotating vortical cells, as previously observed when changing depth.

Here again, the flow along the liquid surface is consistently found radially inward whatever the value of the horizontal aspect ratio. This suggests that, provided the Reynolds number is not larger than 100 typically, a fair approximation of the meridian flow can always be seen as prescribed by mass conservation: the centrifugal force moves the fluid radially outward along the rotating floor and a condition of zero flow rate makes the flow radially inward along the liquid surface, irrespective of the cellular pattern within the core flow.

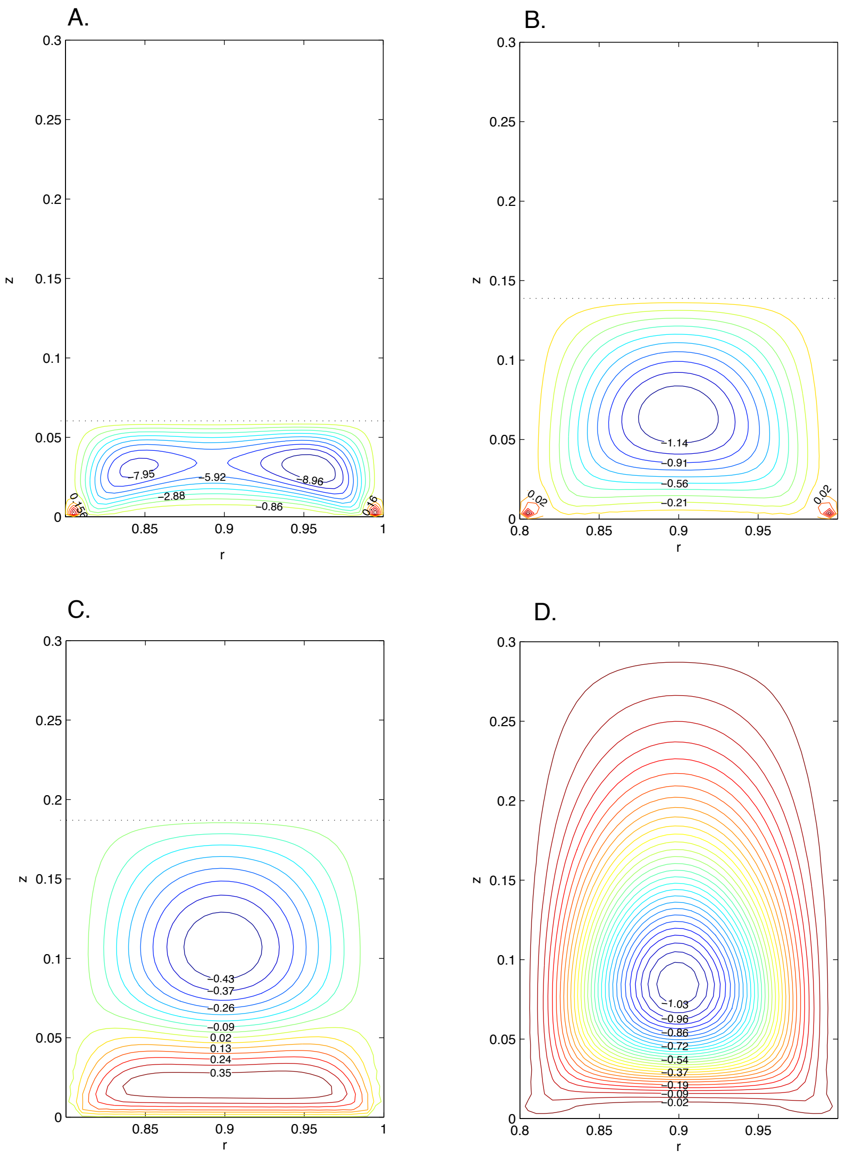

Figure 8. (color online) Streamlines for different values of the vertical aspect ratio with the following horizontal aspect ratio and gap width: $r_i/r_o = 0.8$ and $s = 0.004$. A) $h/r_o = 0.06$. B) $h/r_o = 0.14$. C) $h/r_o = 0.19$. D) $h/r_o = 0.3$. All values along the streamlines when multiplied by 10^6 give the stream function ψ_1.

IV. CONCLUSION

A closed-form solution of an axisymmetric swirling flow in an annular channel, topped with a free surface, has been found, based on a regular asymptotic expansion where Re is a small parameter. With the cylindrical geometry considered, such a flow is made up of two weakly coupled components: a 1-D azimuthal flow, $\vec{v}_\theta\,(r, z)$, and a 2-D meridian flow, $\vec{v}_\perp\,(r, z)$, respectively. Both are explicitly derived as double series of orthogonal eigenfunctions.

Two points should be mentioned: firstly, the asymptotic approximation is valid over a larger range than initially expected, far beyond the Stokes limit, and secondly, the azimuthal and meridian flows are derived from problems at even and odd orders, respectively. This latter feature accounts for how the azimuthal shear flow and the meridian flow interact. It is also demonstrated that the correction at $\mathcal{O}(Re^2)$ to the (azimuthal) Stokes flow is not significant provided that Re $\sim$ 100 at most. In the weakly non linear regime (Re $\sim$ 100 - 800), it is demonstrated to estimate fairly well the azimuthal velocity.

The analytical solution also reveals how the meridian flow patterns can be drastically modified by a change in the

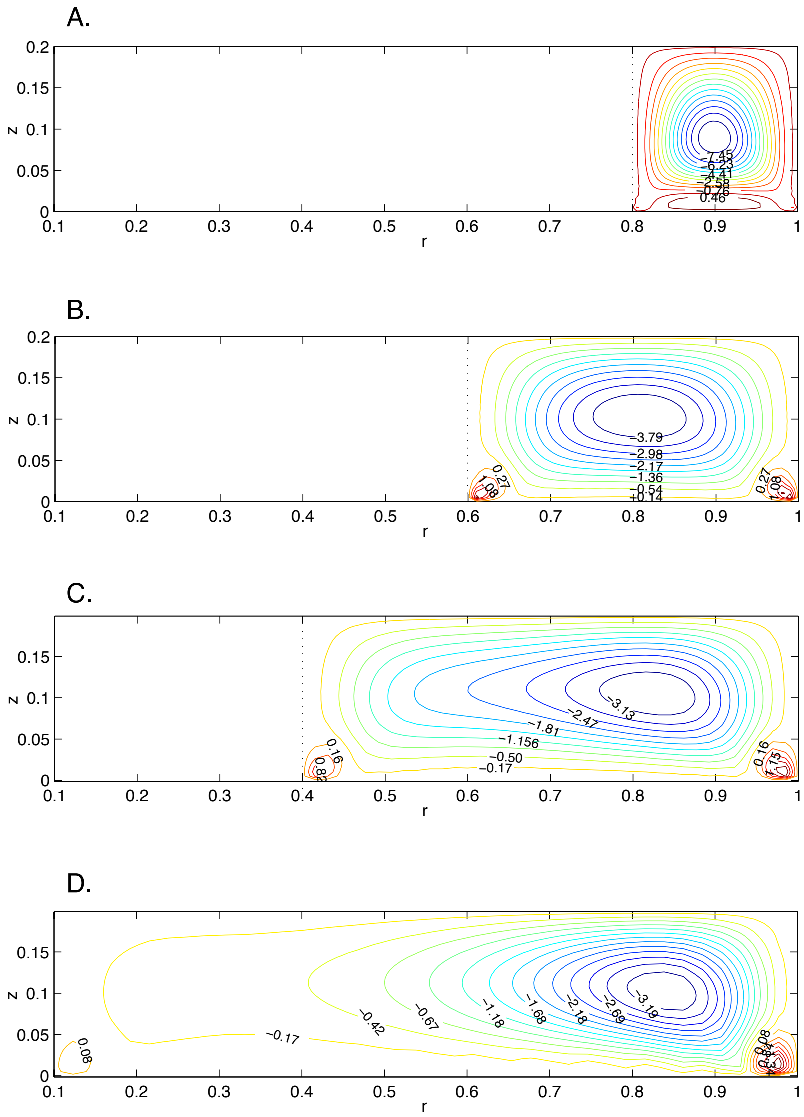

Figure 9. (color online) Streamlines for different values of the horizontal aspect ratio and a fixed vertical aspect ratio, $h/r_o = 0.2$: A) $r_i/r_o = 0.8$ and $s = 0.004$, B) $r_i/r_o = 0.6$ and $s = 0.008$, C) $r_i/r_o = 0.4$ and $s = 0.012$, D) $r_i/r_o = 0.1$ and $s = 0.018$. All values along the streamlines when multiplied by 10^6 give the stream function ψ_1.

horizontal and vertical aspect ratios. As expected from the literature, it is also disrupted by the presence of Moffatt eddies located at corner discontinuities. Due to the linear dependence of the centrifugal force on the radial coordinate, a significant enlargement of the cavity (smaller value of the horizontal aspect ratio) leads to a growing role of the curvature effects and hence, a symmetry break-up of the 2-D recirculating flow, $\overrightarrow{v_\perp}$, in the meridian cross-section. But for a suitable value of the horizontal aspect ratio, close to unity ($r_i/r_o \sim 0.8$), an accurate monitoring of the vertical aspect ratio allows one single vortical flow to be recovered across the channel. More specifically, a significant dependence of this flow pattern on the vertical aspect ratio can be illustrated by three typical cellular patterns which illustrate the competition between the overall influence of centrifugation and the local influence of Moffatt eddies:

- a counter-clockwise co-rotating vortex pair with axis along the radial direction, as observed for a sufficiently small vertical aspect ratio,
- a single vortical cell which prevails as a core flow throughout the cross-section, whose negative vorticity is driven by the centrifugal force. The latter is responsible for a radially outward flow along the rotating floor and, therefore, for a radially inward flow along the free surface due to mass conservation,
- a counter-rotating vortex pair with axis along the vertical direction with the counter-clockwise vortex located

in the upper part of the cavity.

Whatever the flow pattern, its zero flow rate always involves a radially inward flow along the liquid surface.

Our analytical method is proved to take into account a variety of boundary conditions (rotating floor, free surface and stationary walls). Provided that the swirling flow considered is axisymmetric, the extension of the present method to the case of a full cylinder is almost straightforward due to the Neuman condition which holds for ψ along the vertical axis. This is valid irrespective of the boundary conditions at the cavity ends (sliding or rotating covers). This generic ability of our analytical method is essentially due to the introduction of an integral boundary condition for the vorticity ω, which allows the boundary conditions in-excess for ψ to be efficiently redistributed to ω along the side walls and the rotating floor, where no natural boundary condition can be proposed for the vorticity. The problem related to corner discontinuities is also appropriately tackled with this method, which is based on the extensive use of dot products (appendix A). Analytical series we have introduced can be always integrated and the viscous impact of boundary discontinuities upon the flow can be described. All analytical series involved exhibit a rather fast convergence rate, especially when a small lubricated gap is introduced in order to comply with boundary conditions near corners. Introduction of a lubricated gap is probably more realistic than dealing with corner singularities as currently done in the literature. Sensitivity of the azimuthal Stokes flow to gap width has been investigated. A future study could look into how the meridian flow can be affected by small to moderate gaps, using for instance methods developed by Lopez and Chen [31], Piva & Meiburg[36] or Yu *et al.* [37, 38].
To conclude, the present study is intended not only for comparison with numerical codes in asymptotic conditions, but also for monitoring processes based on a confined swirling flow with a free surface above. Present modeling can be extended to surface viscosimetry of 2-D assembly of surfactants molecules [7, 15, 34, 35]) in densified conditions (appendix A).

ACKNOWLEDGMENTS

This work was supported by the French Ministry for Research and Higher Education under ACI Contract PC10-01. The authors gratefully acknowledge Dr. Alain Glière for his valuable assistance in selecting numerical tools.

Appendix A: The case of a contaminated liquid surface

A planar liquid surface contaminated by surfactant molecules. As shown in [16], a strong secondary flow is required to generate a surface velocity with a significant radial component and therefore a nonuniform distribution of surfactant on the interface. Since the flow regime in this paper is at most weakly non linear, the surface dilatational viscosity, the Marangoni effect as well as the radial gradient in surface shear viscosity are disregarded[3]. A (uniform) surface shear viscosity μ_s is introduced by way of a Boussinesq surface fluid model [39] with the following jump momentum balance at the liquid surface ($z = \frac{h}{r_o}$ and $\frac{r_i}{r_o} \leq r \leq 1$):

$$\frac{\partial v_\theta}{\partial z} = \left(1 - \frac{r_i}{r_o}\right) Bo \frac{\partial}{\partial r}\left[\frac{1}{r}\frac{\partial (r v_\theta)}{\partial r}\right]. \tag{A1}$$

Here, the Boussinesq number is referred to as, $Bo = \dfrac{\mu_s}{\mu\,(r_o - r_i)}$, and the gaseous atmosphere is not supposed to yield a significant shearing at the liquid surface [16].

The model to solve writes now:

$$E^2(v_\theta) = Z(v_\theta, \omega, \psi), \tag{A2}$$

completed with the boundary conditions (8) - (10) and (A1). The source term Z either cancels at zeroth order, or writes as $Z = U\,(v_{\theta,0}; \psi_1)$ at $\mathcal{O}(Re^2)$.

The equation (A2) is projected on the set of eigenfunctions $\{q_k(z)\}$ (defined from (28)), using the dot product (33) along the z-axis

$$\frac{\partial^2 v_{\theta_k}}{\partial r^2} + \frac{1}{r}\frac{\partial v_{\theta_k}}{\partial r} - \frac{v_{\theta_k}}{r^2} + \left\langle \frac{\partial^2 v_\theta}{\partial z^2}, q_k \right\rangle_z = Z_k\,(v_\theta, \omega, \psi)\,, \tag{A3}$$

---

[3] Note that these conditions are naturally fulfilled for a highly densified regime (near the maximum packing concentration) or a dilute regime with a large enough surface diffusivity of the surfactant molecules (small surface Peclet number based on the radial velocity).

where $Z\left(v_\theta,\omega,\psi\right)=\sum\limits_{k=1}^{+\infty} Z_k\left(v_\theta,\omega,\psi\right)q_k\left(z\right)$. By making use of the second Green's identity, the latter dot product in (A3) writes:

$$\left\langle \frac{\partial^2 v_\theta}{\partial z^2}, q_k\right\rangle_z = \left\langle v_\theta, \frac{\partial^2 q_k}{\partial z^2}\right\rangle_z + \left[q_k\frac{\partial v_\theta}{\partial z} - v_\theta \frac{\partial q_k}{\partial z}\right]_0^{\frac{h}{r_o}}.$$

Considering that $\frac{\partial^2 q_k}{\partial z^2} = -\gamma_k^2 q_k$, and taking into account (28) as well as the boundary conditions (10), (26) and (27), it can be demonstrated that:

$$\left\langle \frac{\partial^2 v_\theta}{\partial z^2}, q_k\right\rangle_z = -\gamma_k^2 v_{\theta_k} + \sqrt{\frac{2r_o}{h}}(-1)^{k+1}\left.\frac{\partial v_\theta}{\partial z}\right|_{z=\frac{h}{r_o}}$$

$$+\sqrt{\frac{2r_o}{h}}\gamma_k r.$$

Hence, an updated form of (A3) can be writen as:

$$E_r^2(v_{\theta_k}) - \gamma_k^2 v_{\theta_k} = Z_k(v_\theta,\omega,\psi) - \sqrt{\frac{2r_o}{h}}\gamma_k r$$

$$+\sqrt{\frac{2r_o}{h}}(-1)^k\left.\frac{\partial v_\theta}{\partial z}\right|_{z=\frac{h}{r_o}}.$$

Each term v_{θ_k} is now projected on the second set of the eigenfunctions $\{f_j\}$ (as defined from (25)), using the dot product (32) along the r-axis:

$$\left\langle E_r^2(v_{\theta_k}), f_j\right\rangle_r - \gamma_k^2 v_{\theta_{kj}} = Z_{kj}(v_\theta,\omega,\psi) - \sqrt{\frac{2r_o}{h}}\gamma_k\left\langle r, f_j\right\rangle_r$$

$$+\sqrt{\frac{2r_o}{h}}(-1)^k\left\langle \left.\frac{\partial v_\theta}{\partial z}\right|_{z=\frac{h}{r_o}}, f_j\right\rangle_r, \quad \text{(A4)}$$

where $Z_k(v_\theta,\omega,\psi)=\sum\limits_{j=1}^{+\infty} Z_{kj}(v_\theta,\omega,\psi)f_j(r)$ and $\left\langle E_r^2(v_{\theta_k}), f_j\right\rangle_r = -\beta_j^2 v_{\theta_{kj}}$. The latter expression can be demonstrated from the second Green's identity, considering that $E_r^2(f_j) = -\beta_j^2 f_j$ (see eq. (22)), and taking into account (23) as well as the boundary conditions (8) - (9) and (23) - (24). In a similar way, it can be demonstrated that

$$\left\langle \left.\frac{\partial v_\theta}{\partial z}\right|_{z=\frac{h}{r_o}}, f_j\right\rangle_r = \left(\frac{e}{r_o}\right) Bo \int_{\frac{r_i}{r_o}}^{1} r v_\theta(r,\frac{h}{r_o}) E_r^2\left(f_j\right) dr,$$

or equivalently,

$$\left\langle \left.\frac{\partial v_\theta}{\partial z}\right|_{z=\frac{h}{r_o}}, f_j\right\rangle_r = -\left(\frac{e}{r_o}\right) Bo\beta_j^2 v_{\theta_j}(\frac{h}{r_o}),$$

owing to the fact that $E_r^2(f_j) = -\beta_j^2 f_j$. The coefficients $v_{\theta_j}(\frac{h}{r_o})$ in the latter expression can be expanded in a single series as

$$v_{\theta_j}(\frac{h}{r_o}) = \sum_{l=1}^{+\infty} v_{\theta_{lj}} q_l(\frac{h}{r_o}) = \sqrt{\frac{2r_o}{h}}\sum_{l=1}^{+\infty}(-1)^{l+1} v_{\theta_{lj}}.$$

A final expression of (A4) writes as:

$$(\beta_j^2+\gamma_k^2)(-1)^k v_{\theta_{kj}} + \beta_j^2\frac{2r_o}{h}\left(\frac{e}{r_o}\right) Bo\sum_{l=1}^{+\infty}(-1)^l v_{\theta_{lj}} =$$

$$(-1)^k\left[-Z_{k_j}(v_\theta,\omega,\psi) + \sqrt{\frac{2r_o}{h}}\gamma_k\left\langle r, f_j\right\rangle_r\right], \quad \text{(A5)}$$

from which a countable infinite set of vectorial equations can be written and therefore truncated ($k = 1..M$ et $j = 1..N$) to get the required coefficients $v_{\theta_{kj}}$. Hence, the latter expression (A5) writes according to the formulation:

$$\left(\overline{\overline{A_j}} + \beta_j^2 \left(\frac{e}{r_o}\right) \frac{2}{h} Bo \overline{\overline{\Lambda_M}}\right) \left(\overline{v_{\theta_{kj}}} \overrightarrow{u_j}\right) = \overline{\overline{S}} \overrightarrow{u_j},$$

$$\text{for } 1 < j < N,$$

with N, the number of columns, the matrix of coefficients to be calculated, $\overline{v_{\theta_{kj}}} = \left[(-1)^k v_{\theta_{kj}}\right]_{\{k=1...M, j=1...N\}}$, the square matrix of size MxM, $\overline{\overline{A_j}}$,

$$\overline{\overline{A_j}} = \begin{pmatrix} \beta_j^2 + \gamma_1^2 & 0 & \dots & \dots & 0 \\ 0 & \ddots & \ddots & & \vdots \\ \vdots & \ddots & \beta_j^2 + \gamma_k^2 & \ddots & \vdots \\ \vdots & & \ddots & \ddots & 0 \\ 0 & \dots & \dots & 0 & \beta_j^2 + \gamma_M^2 \end{pmatrix},$$

the set of N vectors, $\{\overrightarrow{u_j}\}_{1<j<N}$,

$$\overrightarrow{u_1} = \begin{pmatrix} 1 \\ 0 \\ \vdots \\ 0 \end{pmatrix}, \overrightarrow{u_2} = \begin{pmatrix} 0 \\ 1 \\ 0 \\ \vdots \\ 0 \end{pmatrix}, ..., \overrightarrow{u_N} = \begin{pmatrix} 0 \\ \vdots \\ 0 \\ 1 \end{pmatrix},$$

the NxM source matrix $\overline{\overline{S}}$ with coefficients, $S_{kj} = (-1)^k \left[-Z_{kj}(v_\theta, \omega, \psi) + \sqrt{\frac{2r_o}{h}} \frac{(2k-1)\pi r_o}{2h} \langle r, f_j \rangle_r\right]$, and finally, the square unit matrix, $\overline{\overline{\Lambda_M}}$, of size MxM:

$$\overline{\overline{\Lambda_M}} = \begin{pmatrix} 1 & \dots & \dots & \dots & 1 \\ \vdots & \ddots & & & \vdots \\ 1 & \dots & 1 & \dots & 1 \\ \vdots & & & \ddots & \vdots \\ 1 & \dots & \dots & \dots & 1 \end{pmatrix}.$$

1. Surface flow at leading order

The velocity along a uniformly contaminated liquid surface is calculated at zeroth order (Stokes regime), following the previous steps with $v_{\theta_k} = v_{\theta,0_k}$ and $Z_k(v_\theta, \omega, \psi) = 0$. A comparison with the experimental measurements by Hirsa et al. [14] is displayed in Fig. (10) for $\frac{r_i}{r_o} = 0.77$, $\frac{h}{r_o} = 0.11$, $Bo = 0.027$ and Re=250. Despite the rather large value of the Reynolds number (Stokes regime is eventually questionable, see Fig. 6), a fair agreement is observed in the central area of the liquid surface where velocity scale is recovered. The significant departure between the velocity profiles especially near the side walls could be explained by the radially inward convection of surfactants along the liquid surface in the experiments of Hirsa et al. [14].

2. Considerations on the secondary flow

By considering sequentially the relations (1) and (20), the radial component of the jump momentum balance at $z = \frac{h}{r_o}$,

$$\frac{\partial v_r}{\partial z} = \left(1 - \frac{r_i}{r_o}\right) Bo \frac{\partial}{\partial r}\left[\frac{1}{r}\frac{\partial (r v_r)}{\partial r}\right], \tag{A6}$$

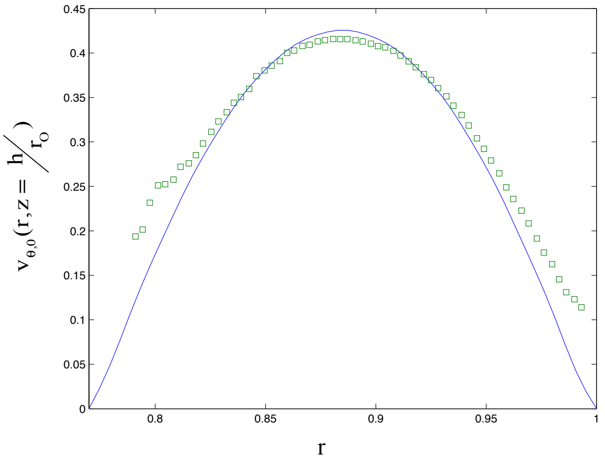

Figure 10. (color online) Comparison along the liquid surface between (□) the experimental data of Hirsa *et al.* [14] and (−) the azimuthal velocity, $v_{\theta,0}(r, h/r_o)$, as calculated at zeroth order ($Z = Z_k\left(v_\theta, \omega, \psi\right) = 0$ in (A2)-(A3)) with $\frac{r_i}{r_o} = 0.77$, $\frac{h}{r_o} = 0.11$, $Bo = 0.027$ and Re=250.

the differential equation (6) and finally the fact that

$$\left.\frac{\partial v_z}{\partial r}\right|_{z=\frac{h}{r_o}} = 0,$$

due to the impermeability condition, $v_z\left(r, z = \frac{h}{r_o}\right) = 0$, it can be demonstrated that a generalized expression of the vorticity at the liquid surface writes:

$$\omega\left(r, z = \frac{h}{r_o}\right) = \left(\frac{r_i}{r_o} - 1\right) Bo \frac{\partial^2}{\partial r \partial z}\left[\frac{1}{r}\frac{\partial\left(r\psi\right)}{\partial r}\right]_{z=\frac{h}{r_o}}. \tag{A7}$$

As made evident from the latter expression, the analytical method developed in this paper is concerned with the dilute regime as a first asymptotic case for which the influence of surfactants becomes negligible (Bo $\rightarrow$ 0). The boundary conditions (18)-(20) are consistently recovered from (A6)-(A7).

As a second asymptotic case, the highly densified regime can be distinguished when the molecular area of the surfactant molecules is so small that $Bo \rightarrow \infty$. Then the jump balance at the surface (A1) simplifies accordingly, $\frac{\partial}{\partial r}\left[\frac{1}{r}\frac{\partial\left(r v_\theta\right)}{\partial r}\right] = 0$, which finally delivers a no-slip condition, $v_\theta = 0$, owing to end conditions at the side walls. Due to continuity equation, $\frac{\partial\left(r v_r\right)}{\partial r} + \frac{\partial\left(v_\theta\right)}{\partial \theta} = 0$, a second no-slip condition is found for the radial velocity, $v_r = 0$ along the liquid surface.
The liquid surface therefore behaves as a wall with the additional boundary condition,

$$\frac{\partial \psi}{\partial z} = 0 \quad \text{at} \quad z = \frac{h}{r_o} \quad \text{along} \quad \frac{r_i}{r_o} < r < 1, \tag{A8}$$

completed by (11)-(13). The integral vorticity condition (34) used in this paper to get the vorticity field, now writes as:

$$\langle\langle \Phi, \omega_1 \rangle\rangle_{r,z} = 0.$$

Based on a new $\omega_{1,j}^{ls}$ sequence assumed to be known along the liquid surface, the condition,

$$\lim_{z \rightarrow \frac{h}{r_o}} \omega\left(r, z\right) = \omega_1^{ls}\left(r\right) = \sum_{j=1}^{+\infty} \omega_{1,j}^{ls} f_j\left(r\right),$$

must be added to the conditions (35)-(37). And following the same route as the one developed in appendix B, a fourth scalar function Φ^{ls} is required in order to check homogeneous boundary conditions everywhere except along the liquid surface.

For any values of Bo, the expression (A7) can not be simplified and introduces an additional coupling between the vorticity and the stream function at the liquid surface. This prevents us to gain benefit from the analytical strategy developed in this paper, essentially based on the fact that the differential equations (5) - (6) and their associated boundary conditions are not two-way coupled at $\mathcal{O}(Re^{(2n+1)})$-orders.
Clearly, the calculation of the $\mathcal{O}$(Re)-order correction to the Stokes flow with a contaminated liquid surface remains beyond the scope of this paper.

Appendix B: Determination of ω_j^f, ω_k^i, ω_k^o sequences at $\mathcal{O}$(Re)

The coefficients $\omega_{1,j}^f$, $\omega_{1,k}^i$ and $\omega_{1,k}^o$ are determined by a proper use of integral boundary condition (34):

$$\langle\langle \Phi, \omega_1 \rangle\rangle_{r,z} = -\left\langle \Phi|_h , \left.\frac{\partial \psi}{\partial z}\right|_{\frac{h}{r_o}} \right\rangle_r , \tag{B1}$$

with well-chosen scalar functions Φ. To this end, three different kind of functions, Φ^f, Φ^i, Φ^o, are defined which boundary conditions differ from each other. First, Φ^f can be introduced in order to check homogeneous boundary conditions everywhere except along the rotating floor:

$$\begin{aligned} \Phi^f = \delta_\Sigma\left(r - r_s\right) = \frac{\delta\left(r-r_s\right)}{r}, \qquad &\text{for } \frac{r_i}{r_o} < r < 1 \\ \text{and } z = 0, \qquad & \end{aligned} \tag{B2}$$

where δ_Σ is the extended Dirac function over this surface.
By inspiring us from the path to get the solution (44) for the vorticity ω_1, one gets here:

$$\Phi^f\left(r,z;r_s\right) = \sum_{j=1}^{+\infty}\sum_{k=1}^{+\infty} \frac{1}{\alpha_k^2+\beta_j^2}\sqrt{\frac{2r_o}{h}}\alpha_k g_k(z) f_j(r) f_j(r_s). \tag{B3}$$

Following the same strategy, the functions Φ^i and Φ^o are required for taking into account homogeneous boundary conditions everywhere except along the inner and outer side walls where:

$$\begin{aligned} \Phi^i = \delta_\Sigma\left(z-z_s\right) = \delta\left(z-z_s\right), & \\ & \text{if } r = \frac{r_i}{r_o} \text{ and } 0 < z < \frac{h}{r_o}, \\ \text{and } \Phi^o = \delta_\Sigma\left(z-z_s\right) = \delta\left(z-z_s\right), & \\ & \text{if } r = 1 \text{ and } 0 < z < \frac{h}{r_o}. \end{aligned}$$

Solutions Φ^i and Φ^o are then found to write:

$$\Phi^i\left(r,z;z_s\right) = \sum_{j=1}^{+\infty}\sum_{k=1}^{+\infty} \frac{\left.\frac{\partial f_j}{\partial r}\right|_{\frac{r_i}{r_o}}}{\alpha_k^2+\beta_j^2} f_j(r) g_k(z) g_k(z_s), \tag{B4}$$

$$\Phi^o\left(r,z;z_s\right) = -\sum_{j=1}^{+\infty}\sum_{k=1}^{+\infty} \frac{\left.\frac{\partial f_j}{\partial r}\right|_{1}}{\alpha_k^2+\beta_j^2} f_j(r) g_k(z) g_k(z_s). \tag{B5}$$

Then considering the term on the right hand side (RHS) of equation (B1), it can be recalled that:

$$\Phi^f\left(r,\frac{h}{r_o};r_s\right) = \Phi^i\left(r,\frac{h}{r_o};z_s\right) = \Phi^o\left(r,\frac{h}{r_o};z_s\right) = 0,$$

which leads to:

$$0 = \left\langle \Phi^f\big|_{\frac{h}{r_o}}, \left.\frac{\partial \psi}{\partial z}\right|_{\frac{h}{r_o}} \right\rangle_r = \left\langle \Phi^i\big|_{\frac{h}{r_o}}, \left.\frac{\partial \psi}{\partial z}\right|_{\frac{h}{r_o}} \right\rangle_r$$

$$= \left\langle \Phi^o\big|_{\frac{h}{r_o}}, \left.\frac{\partial \psi}{\partial z}\right|_{\frac{h}{r_o}} \right\rangle_r .$$

Thus, injecting expression (44) and sequentially (B3), (B4), (B5) in (B1) leads to:

$$\sum_{j=1}^{+\infty}\sum_{k=1}^{+\infty} a^f_{kj} \left[h_{1,kj} + \omega^i_{1,k} \left.\frac{\partial f_j}{\partial r}\right|_{\frac{r_i}{r_o}} - \omega^o_{1,k} \left.\frac{\partial f_j}{\partial r}\right|_1 + \sqrt{\tfrac{2r_o}{h}}\alpha_k \omega^f_{1,j} \right]$$

$$.\ f_j(r_s) = 0, \tag{B6}$$

$$\sum_{j=1}^{+\infty}\sum_{k=1}^{+\infty} a^i_{kj} \left[h_{1,kj} + \omega^i_{1,k} \left.\frac{\partial f_j}{\partial r}\right|_{\frac{r_i}{r_o}} - \omega^o_{1,k} \left.\frac{\partial f_j}{\partial r}\right|_1 + \sqrt{\tfrac{2r_o}{h}}\alpha_k \omega^f_{1,j} \right]$$

$$.\ g_k(z_s) = 0, \tag{B7}$$

$$\sum_{j=1}^{+\infty}\sum_{k=1}^{+\infty} a^o_{kj} \left[h_{1,kj} + \omega^i_{1,k} \left.\frac{\partial f_j}{\partial r}\right|_{\frac{r_i}{r_o}} - \omega^o_{1,k} \left.\frac{\partial f_j}{\partial r}\right|_1 + \sqrt{\tfrac{2r_o}{h}}\alpha_k \omega^f_{1,j} \right]$$

$$.\ g_k(z_s) = 0, \tag{B8}$$

with:

$$a^f_{kj} = \sqrt{\frac{2r_o}{h}} \frac{k\pi r_o}{h} \frac{1}{\left(\alpha_k^2 + \beta_j^2\right)^2}, \tag{B9}$$

$$a^i_{kj} = \frac{1}{\left(\alpha_k^2 + \beta_j^2\right)^2} \left.\frac{\partial f_j}{\partial r}\right|_{\frac{r_i}{r_o}}, \tag{B10}$$

$$a^o_{kj} = \frac{1}{\left(\alpha_k^2 + \beta_j^2\right)^2} \left.\frac{\partial f_j}{\partial r}\right|_1 . \tag{B11}$$

A countable infinite equations ($j = 1... + \infty$, $k = 1.. + \infty$) is obtained by operating dot products (defined in 32 and 33) of (B6) with $f_j(r_s)$ and dot products of (B7) and (B8) with $g_k(z_s)$. Truncation to orders $j = M$, $k = N$ gives $(M + 2N)$ linear equations which permit *in fine* to find the series of coefficients $\omega^i_{1,k}$, $\omega^o_{1,k}$, $\omega^f_{1,j}$:

$$\omega^f_{1,j} \sum_{k=1}^{N} \sqrt{\frac{2r_o}{h}} \alpha_k a^f_{kj} + \left.\frac{\partial f_j}{\partial r}\right|_{\frac{r_i}{r_o}} \sum_{k=1}^{N} a^f_{kj}\omega^i_{1,k} - \left.\frac{\partial f_j}{\partial r}\right|_1 \sum_{k=1}^{N} a^f_{kj}\omega^o_{1,k} = -\sum_{k=1}^{N} a^f_{kj} h_{1,kj}, \tag{B12}$$

$$\sqrt{\frac{2r_o}{h}} \alpha_k \sum_{j=1}^{M} a^i_{kj}\omega^f_{1,j} + \omega^i_{1,k} \sum_{j=1}^{M} a^i_{kj} \left.\frac{\partial f_j}{\partial r}\right|_{\frac{r_i}{r_o}} - \omega^o_{1,k} \sum_{j=1}^{M} a^i_{kj} \left.\frac{\partial f_j}{\partial r}\right|_1 = -\sum_{j=1}^{M} a^i_{kj} h_{1,kj}, \tag{B13}$$

$$\sqrt{\frac{2r_o}{h}} \alpha_k \sum_{j=1}^{M} a^o_{kj}\omega^f_{1,j} + \omega^i_{1,k} \sum_{j=1}^{M} a^o_{kj} \left.\frac{\partial f_j}{\partial r}\right|_{\frac{r_i}{r_o}} - \omega^o_{1,k} \sum_{j=1}^{M} a^o_{kj} \left.\frac{\partial f_j}{\partial r}\right|_1 = -\sum_{j=1}^{M} a^o_{kj} h_{1,kj}. \tag{B14}$$

---

[1] M. Escudier, Exp. Fluids **2**, 189 (1984).
[2] A. Spohn, M. Mory, and E. Hopfinger, Exp. Fluids **14**, 70 (1993).
[3] A. Spohn, M. Mory, and E. Hopfinger, J. Fluid Mech. **370**, 73 (1998).
[4] M. Brons, L. Voigt, and J. Sorensen, J. Fluid Mech. **428**, 133 (2001).
[5] F. Sotiropoulos and Y. Ventikos, J. Fluid Mech. **426**, 155 (2001).

[6] J. M. Lopez, F. Marques, A. H. Hirsa, and R. Miraghaie, J. Fluid Mech. **502**, 99 (2004).
[7] A. Azadani, J. M. Lopez, and A. H. Hirsa, Langmuir **23**, 5227 (2007).
[8] D. Lo Jacono, M. Nazarinia, and M. Brns, Phys. Fluids **21**, 111704 (2009).
[9] A. Khalili and H. Rath, ZAMP **45**, 670 (1994).
[10] C. P. Hills, Phys. Fluids **13**, 2279 (2001).
[11] B. K. Muite, Phys. Fluids **16**, 3614 (2004).
[12] T. Duffar, *Crystal Growth Processes Based on Capillarity: Czochralski, Floating Zone, Shaping and Crucible Techniques* (Wiley-Blackwell, 2010).
[13] A. H. Hirsa, J. M. Lopez, and R. Miraghaie, J. Fluid Mech. **443**, 271 (2001).
[14] A. H. Hirsa, J. M. Lopez, and R. Miraghaie, J. Fluid Mech. **470**, 135 (2002).
[15] L. Davoust, Y.-L. Huang, and S.-H. Chang, Phys. Fluids **20**, 082105 (2008).
[16] J. M. Lopez and A. Hirsa, J. Colloid Interface Sci. **206**, 231 (1998).
[17] J. M. Lopez, R. Miraghaie, and A. H. Hirsa, J. Colloid Interface Sci. **248**, 103 (2002).
[18] V. Shtern, J. Fluid Mech. **711**, 667 (2012).
[19] V. Shtern, Phys. Fluids **25**, 083604 (2013).
[20] J. Sturzenegger, L. Sarasua, and A. C. Marti, Journal of Fluids and Structures **28**, 473 (2012).
[21] L. Davoust, Y.-L. Huang, and S.-H. Chang, Surface Science **603**, 2777 (2009).
[22] J. Delacroix and L. Davoust, Phys. Fluids **26**, 037102 (2014).
[23] A. Nayfeh, *Perturbation methods*, 1st ed., Pure and applied mathematics (Wiley Interscience, New York, 1973).
[24] E. J. Hinch, *Perturbation methods* (Press Syndicate of the University of Cambridge, Cambridge, 1991).
[25] R. J. Manheimer and R. S. Schechter, J. Colloid Interface Sci. **32**, 195 (1970).
[26] L. Quartapelle and F. Valz-Gris, Int. J. Numer. Meth. Fluids **1**, 129 (1981).
[27] I. S. Gradhsteyn and I. M. Ryzhik, *Tables of integrals, series and products* (Academic, New York, 1965).
[28] A. J. Pintar, *The measurement of surface viscosity*, Ph.D. thesis, Illinois Institute of Technology (1968).
[29] L. Drazek, *Contrôle par l'hydrodynamique de l'assemblage 2-D de protéines dans une interface eau-air. Modélisation, premieres expériences*, Ph.D. thesis, Univ. Grenoble-Alpes (2004).
[30] J. M. Lopez, J. Fluid Mech. **359**, 49 (1998).
[31] J. M. Lopez and J. Chen, J. Comp. Phys. **139**, 308 (1998).
[32] H. K. Moffatt, J. Fluid Mech. **18**, 1 (1964).
[33] H. Moffatt, *Singularities in Fluid Dynamics and their Resolution*, Lectures on Topological Fluid Mechanics (Springer Berlin Heidelberg, 2009) pp. 157–166.
[34] L. Drazek, J.-F. Legrand, and L. Davoust, J. Crystal Growth **275**, e1467 (2005).
[35] A. H. Sadoughi, J. M. Lopez, and A. H. Hirsa, Phys. Fluids **25**, 032107 (2013).
[36] M. Piva and E. Meiburg, Phys. Fluids **17**, 063603 (2005).
[37] P. Yu, T. S. Lee, Y. Zeng, and H. T. Low, Phys. Fluids **19**, 057104 (2007).
[38] P. Yu, Y. Zeng, T. S. Lee, and H. T. Low, Phys. Fluids **20**, 087103 (2008).
[39] J. C. Slattery, L. Sagis, and E.-S. Oh, *Interfacial transport phenomena.* 2^{nd} *Edition* (Springer-Verlag, 1990).